Determination of field output correction factors in elongated small field photon beams

Miss Mananchaya Vimolnoch

A Dissertation Submitted in Partial Fulfillment of the Requirements

for the Degree of Doctor of Philosophy in Medical Physics

Department of Radiology

FACULTY OF MEDICINE

Chulalongkorn University

Academic Year 2021

การหาค่าแก้เอาท์พุทแฟคเตอร์สำหรับลำรังสีโฟตอนที่มีพื้นที่รังสีแนวยาวขนาดเล็ก

น.ส.มนัญชยา วิมลโนช

Thesis Title	Determination of field output correction factors
	in elongated small field photon beams
By	Miss Mananchaya Vimolnoch
Field of Study	Medical Physics
Thesis Advisor	Sornjarod Oonsiri

Accepted by the FACULTY OF MEDICINE, Chulalongkorn University in Partial Fulfillment of the Requirement for the Doctor of Philosophy

.... Dean of the FACULTY OF MEDICINE

(Associate Professor CHANCHAI SITTIPUNT, M.D.)

DISSERTATION COMMITTEE

.... Chairman

(Associate Professor ANCHALI KRISANACHINDA, Ph.D.)

.... Thesis Advisor

(Sornjarod Oonsiri)

.... Examiner

(Assistant Professor TAWEAP SANGHANGTHUM, Ph.D.)

.... Examiner

(Assistant Professor YOTHIN RAKVONGTHAI, Ph.D.)

.... External Examiner

(Professor Jan P Seuntjens, Ph.D.)

มนัญชยา วิมลโนช : การหาค่าแก้เอาท์พุทแฟคเตอร์สำหรับลำรังสีโฟตอนที่มีพื้นที่รังสีแนวยาวขนาดเล็ก. (Determination of field output correction factors in elongated small field photon beams) อ.ที่ปรึกษาหลัก : ดร.สรจรส อุณห์ศิริ

ไอเออีเอ (IAEA) และ เอเอพีเอ็ม (AAPM) ได้ตีพิมพ์ทีอาร์เอส (TRS) 483 เป็นมาตรฐานสำหรับการวัดปริมาณรังสีสำหรับพื้นที่รังสีขนาดเล็ก ซึ่งมีค่าแก้ฟิลด์เอาท์พุตแฟคเตอร์ (field output facto)r สำหรับหัวรังสีหลายชนิด สามารถนำมาแก้ค่าการตอบสนองต่อรังสีของหัววัดที่เปลี่ยนไปเวลาวัดปริมาณรังสีแบบสัมพัทธ์ (relative) อย่างไรก็ตามค่าแก้ในทีอาร์เอส 483 มีเฉพาะพื้นที่ลำรังสีสมมาตรเป็นสี่เหลี่ยมจตุรัสเท่านั้น ไม่มีค่าแก้สำหรับลำรังสีที่มีพื้นที่ไม่สมมาตรลักษณะแนวยาว วัตถุประสงค์ของการศึกษานี้คือการหา ค่าฟิลด์เอาท์พุตแฟคเตอร์เมื่อพื้นที่ลำรังสีมีลักษณะแนวยาวขนาดเล็ก การศึกษาเริ่มจากการหาค่าแก้ของหัววัดรังสีสามชนิดได้แก่ หัววัดชนิดไอออไนเซชั่น ซีซีโอวัน (Ionization chamber CC01) หัววัดชนิดไดโอด เอดจ์ (EDGE diode detector) และ หัววัดชนิดพลาสติกเปล่งแสง เอ็กราดิน ดับบลิวทู (Plastic scintillator Exradin W2) ที่ลำรังสีโฟตอนพลังงาน 6 เม็กกะโวลต์ (MV) โดยใช้การจำลองมอนตี คาร์โล (Monte Carlo simulation) มีการคำนวณอัตราส่วนของปริมาณรังสีดูดกลืนในน้ำและในหัววัดรังสีโดยใช้โค้ด อีจีเอสแชมเบอร์ (egs_chamber) ที่ระยะจากแหล่งกำเนิดรังสีถึงผิวเท่ากับ 90 เซนติเมตรและความลึก 10 เซนติเมตร พื้นที่รังสีแนวยาวขนาดเล็กที่ใช้ในการคำนวนคือ 3x2 2x3 1.5x4 4x1.5 1x6 6x1 0.6x10 และ 10x0.6 ตารางเซนติเมตร มีเฟสสเปซไฟล์ (phase-space file) ของเครื่องเร่งอนุภาคทรูบีม (TrueBeam™) จากบริษัทแวเรียน (Varian) เป็นแหล่งกำเนิดรังสี มีการตรวจสอบค่าแก้ที่คำนวณได้โดยการวัดค่าฟิลด์เอาท์พุตแฟคเตอร์ (Field output factor; FOF) โดยใช้หัววัดรังสี พื้นที่ลำรังสี เครื่องเร่งอนุภาคชนิดเดียวกับที่ทำการจำลองมอนติ คาร์โล มีการเปรียบเทียบค่าฟิลด์เอาท์พุตแฟคเตอร์ ที่ใช้ค่าแก้จากการศึกษานี้และค่าแก้จาก TRS 483 โดยใช้เปอร์เซนต์ส่วนเบี่ยงเบนมาตรฐาน (%SD) ในการประเมิน จากการศึกษาพบว่าสำหรับพื้นที่ลำรังสีขนาด 3x2 2x3 1.5x4 และ 4x1.5 ตารางเซนติเมตรมีค่า %SD สูงที่สุดเท่ากับ 1.1% เมื่อฟิลด์เอาท์พุตแฟคเตอร์ ไม่ถูกแก้ค่า ส่วนฟิลด์เอาท์พุตแฟคเตอร์ ที่ใช้ค่าแก้จากการศึกษานี้และทีอาร์เอส 483 ให้ค่า %SD ที่เทียบเคียงกันเท่ากับ 0.6% สำหรับพื้นที่รังสีลักษณะเป็นแนวยาวขนาดเล็กอย่างมาก (1x6 6x1 0.6x10 และ 10x0.6 ตารางเซนติเมตร) พบ %SD สูงที่สุดเท่ากับ 7.3% เมื่อฟิลด์เอาท์พุตแฟคเตอร์ไม่ถูกแก้ค่า และลดลงเหลือ 3.8% เมื่อฟิลด์เอาท์พุตแฟคเตอร์ ใช้ค่าแก้จากการศึกษานี้ ในทางกลับกัน %SD มีค่าเท่ากับ 6.9% เมื่อใช้ค่าแก้จาก TRS 483 จากการศึกษาค่าแก้ของหัววัดรังสีแต่ละชนิดพบว่า หัววัดรังสีซีซีโอวัน ให้ค่าแก้ที่สูงถึง 7% สำหรับด้านที่เล็กที่สุดของลำรังสีเนื่องจาก volume averaging effect ส่วนหัววัดรังสีชนิดไดโอด เอดจ์ ให้ค่าแก้ต่ำเท่ากับ -3% สำหรับหัววัดชนิดพลาสติกเปล่งแสง เอ็กราดิน ดับบลิวทู ให้ค่าแก้ที่อยู่ใน 1% ถึงแม้ว่าพื้นที่ลำรังสีนั้นจะมีลักษณะเป็นแนวยาวขนาดเล็กอย่างมากก็ตาม เนื่องมากจากหัววัดรังสีชนิดนี้มีคุณสมบัติเทียบเท่าน้ำ การเลือกค่าแก้ฟิลด์เอาท์พุตแฟคเตอร์ ในทีอาร์เอส 483 ถูกกำหนดโดยด้านของพื้นที่รังสีจัตุรัสขนาดเล็ก (equivalent square small field ;) วิธีนี้สามารถใช้ได้เมื่อพื้นที่ลำรังสีมีลักษณะสมมาตร มีอัตราส่วนของด้านกว้างและยาวอยู่ในช่วง 0.7-1.4 ผลการศึกษาพบว่า อัตราส่วนของกว้างและยาวสามารถขยายได้ถึง 0.3-2.5 เนื่องจาก %SD ของพื้นที่ลำรังสี 1.5x4 และ 4x1.5 ตารางเซนติเมตรมีค่าน้อยกว่า 1% เมื่อใช้ค่าแก้จากการศึกษานี้และจากทีอาร์เอส 483 อย่างไรก็ตามเมื่อพื้นที่ลำรังสีเป็นแนวยาวและเล็กอย่างมาก ไม่สามารถนำมาใช้ในการเลือกค่าแก้ในทีอาร์เอส 483 ได้จึงต้องมีการหาค่าแก้ของพื้นที่ลำรังสีเหล่านี้โดยใช้วิธีตามที่ทีอาร์เอส 483 กำหนด

สาขาวิชา	ฟิสิกส์การแพทย์	ลายมือชื่อนิสิต ....
ปีการศึกษา	2564	ลายมือชื่อ อ.ที่ปรึกษาหลัก ....

Mananchaya Vimolnoch : Determination of field output correction factors in elongated small field photon beams. Advisor: Dr. Sornjarod Oonsiri

IAEA along with AAPM have published a code of practice TRS 483 for small field dosimetry. The field correction output factors of various detectors were introduced to correct detector response changes in relative dosimetry. However, the publication of TRS 483 has focused on symmetry field sizes, the correction factors for elongated small fields are not included in the protocol. The overall objective of this work is to determine the field output correction factor in elongated small field. The correction factors of IBA CC01, Sun nuclear EDGE, and Exradin W2 PSD for 6 MV photon beam were determined using Monte Carlo (MC) simulation. The ratio of absorbed dose of water and of detectors was calculated using egs_chamber code, both at a depth of 10 cm with 90 cm SSD. The elongated field sizes were 3x2, 2x3, 1.5x4, 4x1.5, 1x6, 6x1, 0.6x10, and 10x0.6 cm^2. The phase-space files from a Varian TrueBeam^{TM} were used as a particle source. The calculated correction factors from this study were verified against the experiment. The field output factors (FOF) were measured using the same detectors, field sizes, and linear accelerator machine that were simulated with MC method. The comparison between FOF corrected with our correction factor and from TRS 483 was analyzed using percent standard deviation (%SD). For 3x2, 2x3, 1.5x4, and 4x1.5 cm^2, the maximum %SD of uncorrected FOF was 1.1%. The FOF corrected with our correction factors and TRS 483 give the comparable %SD of 0.6%. For extremely elongated field sizes (1x6, 6x1, 0.6x10, and 10x0.6 cm^2), the maximum %SD was 7.3% for uncorrected FOF. When our correction factors were applied, this value dropped to 3.8%. In contrast, the corrected FOF with TRS 483 gives the %SD of 6.9%. For IBA CC01 ionization chamber the correction factors were up to 7% for the smallest side of the fields, the most important contribution to the correction factor is volume averaging effect. The correction factors for Edge detector were of the order of -3% for the smallest side of the fields. The W2 PSD the correction factors are within 1% even for extremely elongated fields due to water equivalence characteristics. TRS 483 recommended to determine the for selecting the correction factor when the field is not too elongated with the ratio of Y/X FWHM in the range between 0.7-1.4. Our results show that the range may be extended up to 0.3-2.5 due to the %SD was less than 1% when the FOF was corrected with either our correction factor or TRS 483 for 1.5x4 and 4x1.5 cm^2. However, when the field size becomes extremely elongated, the definition of equivalent square small field size ( ) is no longer hold. Then, the correction factor should be determined follow TRS 483.

Field of Study:	Medical Physics	Student's Signature	
Academic Year:	2021	Advisor's Signature	

ACKNOWLEDGEMENTS

TABLE OF CONTENTS

จุฬาลงกรณ์มหาวิทยาลัย

CHULALONGKORN UNIVERSITY

LIST OF TABLES

LIST OF FIGURES

จุฬาลงกรณ์มหาวิทยาลัย

CHULALONGKORN UNIVERSITY

LIST OF ABBREVIATIONS AND SYMBOLS

AAPM	American Association of Physicists in Medicine
CE	Collimator exchange effect
CLR	Čerenkov Light Ratio
CPE	Charged particle equilibrium
d	Largest dimension of the detector's outer boundary
DTA	Distance to agreement
d_{max}	Depth of maximum dose
D_w	Absorbed dose to water
$D_{w,Q_{ref}}^{f_{ref}}$	Absorbed dose to water in reference field
$D_{w,Q_{clin}}^{f_{clin}}$	Absorbed dose to water in any clinical field
E	Equivalent square field
EGS	Electron Gamma Shower
FOF	Field output factor
f_{clin}	clinical field size
f_{ref}	reference field size
FWHM	Full width half maximum
IAEA	International Atomic Energy Agency
IMRT	Intensity Modulated Radiation Therapy
$K_{col,w}$	Water collision kerma
$k_{Q_{clin},Q_{msr}}^{f_{clin},f_{msr}}$	Field output correction factor
k_{MC}	Field output correction factor calculated from this study
k_{TRS}	Field output correction factor tabulated in TRS 483
LCPE	Lateral electronic equilibrium
msr	Machine specific reference field
MLC	Multileaf collimator
MC	Monte Carlo
$M_{w,Q_{ref}}^{f_{ref}}$	Meter reading to water in reference field
$M_{w,Q_{clin}}^{f_{clin}}$	Meter reading to water in clinical field
OF	Output factor
PDD	Percentage depth dose

PSD	Plastic scintillator detector
q_{clin}	Beam quality of clinical field
q_{ref}	Beam quality of reference field
r_{LCPE}	Lateral charged particle equilibrium
SRS	Stereotactic radiosurgery
SRT	Stereotactic Radiation Therapy
SBRT	Stereotactic body radiation therapy
S_{clin}	Equivalent square small field size
$SC(r)$	Central axis scatter dose in a circular field of radius r
$SC(\infty)$	Central axis scatter dose in field of infinite radius
$TPR_{20,10}(10)$	Tissue-phantom ratio in water at depths of 20 and 10 g/cm^2 at 10×10 cm^2
TRS	Technical Reports Series
VMAT	Volumetric Modulated Arc Therapy
$\Omega_{Q_{clin},Q_{msr}}^{f_{clin},f_{msr}}$	Field output factor
λ	Scale parameter of dimensions length
μ	Dimensionless shape parameter lying between 0 and 1
%SD	Percent standard deviation

CHAPTER 1

INTRODUCTION

1.1 Background and Rationale

Recent advanced techniques in photon beam radiotherapy have been developed to improve the accuracy of radiation delivery with very fast treatment times. These advances have given rise to the increased use of small fields over the past decades. Using small radiation fields allows a large amount of dose to be irradiated in the tumor and, at the same time, avoids healthy tissue for improved control of the disease. The small fields are implemented with various treatment forms of stereotactic radiotherapy (SRT), stereotactic body radiotherapy (SBRT), stereotactic radiosurgery (SRS), and intensity modulated radiotherapy (IMRT). These are performed with a variety of linear accelerators and specialized machines such as TomoTherapy®, CyberKnife®, and Gamma Knife®. The field size is designated small with different collimation types, including jaws, multileaf collimator (MLC), cones, and adjustable tertiary collimators.

Despite its advantage, these small field measurements are challenging due to one or more of its three conditions (1): The first condition is lack of lateral electronic equilibrium (LCPE). This occurs when half of the field size is smaller than the range of the lateral charged particle equilibrium (r_{LCPE}). The second condition is a source occlusion by the collimator device, resulting in an overlapping of the penumbra. Both conditions lead to a sharp drop in beam output. Then, the irradiation field becomes boarder than the geometrical field size defined by the collimator devices. The third condition is associated with a detector for a given field. These conditions are associated with the volume averaging at the high-gradient dose distributions and the perturbation of fluence photons arising from the different physical densities between detector and medium.

According to small field characteristics, measuring the field output factor ($\Omega_{Q_{clin},Q_{msr}}^{f_{clin},f_{msr}}$) for small fields need to be concerned. Field output factor is defined as the ratio of absorbed dose to water in any clinical field to that in a reference field at a given depth. In board beam, $\Omega_{Q_{clin},Q_{msr}}^{f_{clin},f_{msr}}$ is determined using a ratio of detector readings ($M_{Q_{clin}}^{f_{clin}}/M_{Q_{msr}}^{f_{msr}}$) since the dosimetric quantities are independent of field size. For small fields, it is obvious that the ratio of the detector reading is not equal to the ratio of absorbed dose. Then, the output correction factor ($k_{Q_{clin},Q_{msr}}^{f_{clin},f_{msr}}$) is introduced to correct the differences in a detector response between the clinical and reference fields.

In 2017, the International Atomic Energy Agency (IAEA) along with the American Association of Physicists in Medicine (AAPM) have published Technical Reports Series number 483 (TRS 483) (2)

that provides a code of practice (CoP) for small field dosimetry. TRS 483 provided recommendations for small field measurement and values of the $k_{Q_{clin},Q_{msr}}^{f_{clin},f_{msr}}$ to multiply with the ratio of detector readings for accurately determination of the $\Omega_{Q_{clin},Q_{msr}}^{f_{clin},f_{msr}}$ as supplied by Equation1.1

$$\Omega_{Q_{clin},Q_{msr}}^{f_{clin},f_{msr}} = \left(\frac{M_{Q_{clin}}^{f_{clin}}}{M_{Q_{msr}}^{f_{msr}}}\right) \times k_{Q_{clin},Q_{msr}}^{f_{clin},f_{msr}} \tag{1.1}$$

Since the geometrical field size from collimator settings cannot represent the dosimetric field in a small field, Cranmer-Sargison *et al.* (3) introduced the equivalent square small field size (S_{clin}) which later adopted in TRS 483 for selecting the $k_{Q_{clin},Q_{msr}}^{f_{clin},f_{msr}}$ for each small field size. The S_{clin} of small rectangular fields with uneven in-plane and cross-plane full width at half maximum (FWHM) is given by Equation1.2

$$S_{clin} = \sqrt{A \times B} \tag{1.2}$$

Where A and B is the radiation field width in the in-plane direction and cross-plane direction, respectively.

The concept of the S_{clin} can be applied to field size that is not too elongated, which A/B fall within 0.7-1.4. When the field sizes are extremely asymmetric or when A/B could not fall between those limits. Then S_{clin} cannot be specified lead to the selection of $k_{Q_{clin},Q_{msr}}^{f_{clin},f_{msr}}$ for extremely asymmetric fields are omitted. Depending on the treatment planning system (TPS) used, $\Omega_{Q_{clin},Q_{msr}}^{f_{clin},f_{msr}}$ of a small elongated field may be used as the entry data for dose calculation. There is thus a need for the development of a criterion to specify an equivalent small field size for these elongated fields. Recently most of the published papers were focused on dosimetry in small symmetric fields. The information on small elongated fields is limited. To fill in the gap of TRS 483, the overall objective of this work is to determine $k_{Q_{clin},Q_{msr}}^{f_{clin},f_{msr}}$ of the elongated small field that only one of the sides of the field is below twice lateral equilibrium electron range.

1.2 The scope of the thesis

This research covers the measurements of the $\Omega_{Q_{clin},Q_{msr}}^{f_{clin},f_{msr}}$ in small elongated fields using several detectors and the study of the $k_{Q_{clin},Q_{msr}}^{f_{clin},f_{msr}}$ as a function of the small field definition proposed in TRS 483.

1.3 Keywords

Elongated small field photon beam, Field output factor, Field output correction factor, equivalent square field, egs_chamber, Monte Carlo simulation.

CHAPTER 2

REVIEWS OF RELATED LITERATURE

2.1 Theories

2.1.1 Small field condition

A small field is defined as a field with a size smaller than the twice lateral secondary electron range that contributes to the absorbed dose. According to this criteria, the field size that is considered small for 6 MV photon beams is when the field below 3×3 cm^2.

Small fields are those meeting one of the following conditions (2).

(i) Loss of lateral charged particle equilibrium (LCPE) on the beam axis

(ii) Partial occlusion of the photon source by the collimating devices on the beam axis;

(iii) The size of the detector is large compared to the field size.

The first two conditions are related to the beam, while the last condition is associated with the detector's selection.

(i) Loss of LCPE on the beam axis

Charged particle equilibrium (CPE) is the condition when the secondary electrons leaving a volume of interest are replaced by an equal number of the secondary electrons of the same type and energy, leading to the deposited energy of the secondary electron entering and leaving the volume are balance (4). As long as the CPE exists, the water collision kerma ($K_{col,w}$) is equal to the absorbed dose to water (D_w). Typically, for broad MV photon beams, CPE occurs in both directions; longitudinal and lateral. When the photon beam is too small in the lateral dimension, the leaving the secondary electrons are not compensated by the entering electrons, leading to the failure of LCPE. This happens when the photon beam half width is smaller than the maximum range of the secondary electrons. Figure 2.1 shows the ratio of D_w and $K_{col,w}$ from different beam energy as a function of field radius. The loss of LCPE appears when $D_w/K_{col,w}$ is less than unity. Using higher energy, the field radius that can maintain LCPE need to be larger since the range of the secondary electron is increased.
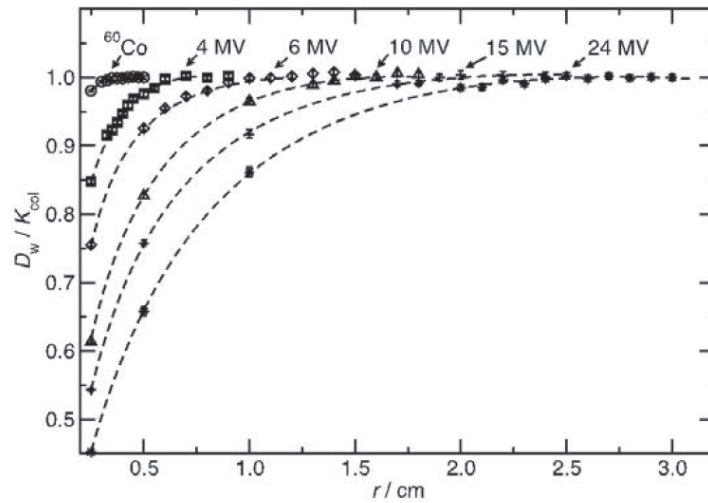
Figure 2.1 Ratios of absorbed dose and collision kerma to water ($D_w/K_{col,w}$) calculated by Monte Carlo simulation. The data are plotted as a function of the field size radius of difference energies photon beams. Figure from TRS 483.

To identify if a radiation field size is small, a practical parameter named the LCPE range (r_{LCPE}) is used. The r_{LCPE} is defined as the minimum radius of a circular photon field for which $K_{col,w} = D_w$ at the center of the field size. It is given in the TRS 483 by

$$r_{LCPE}(cm) = 8.369 \times TPR_{20,10}(10) - 4.382 \qquad (2.1)$$

When $TPR_{20,10}(10)$ is tissue phantom ratio in water at depths of 20 and 10 g/cm^2 at a field size of 10×10 cm^2 with source to detector distance (SDD) of 100 cm. This factor is used as used the photon beam quality index. For 6 MV photon beam with $TPR_{20,10}(10)$ of 0.67, the r_{LCPE} equals to 1.22 cm. Then, the field is considered to be small when its size is shorter than 2.45 x 2.45 cm^2.

(ii) Partial occlusion of the photon source by the collimating devices on the beam axis

The condition occurs when the finite primary photon source is obscured by the collimator of a linear accelerator, and only a part of the source area can be seen from the point of measurement, as presents in Figure 2.2
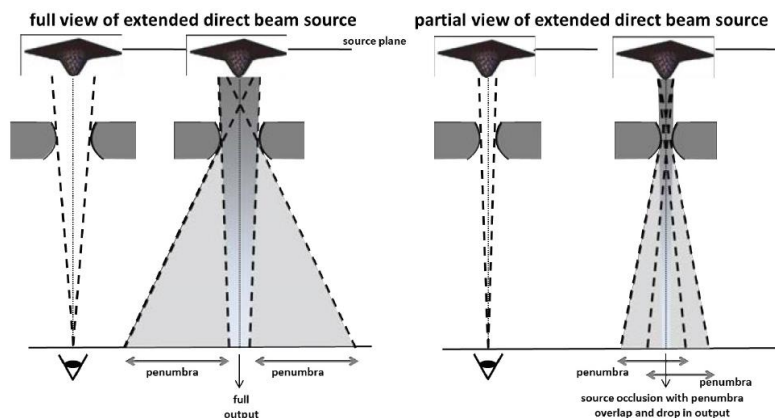
Figure 2.2 Schematic illustration of the source occlusion effect. The left figure represents a large photon beam where the primary source is not obscure by the collimator, and there is a clear distinction between the radiation field and the penumbra region. The right shows the situation of partial source occlusion in a small photon beam where the penumbra is overlapping. Figure from TRS 483

The source occlusion effect becomes significant when the field size is smaller or comparable to the size of the photon source, which has a size < 5 mm for present linear accelerators. The primary source occlusion results in not only the overlap of penumbra and lower beam output but also the widening of the apparent field width. Figure 2.3 illustrates this situation which causes the discrepancy between nominal field size defined by collimator setting and radiation field size described at the full width at half maximum (FWHM).
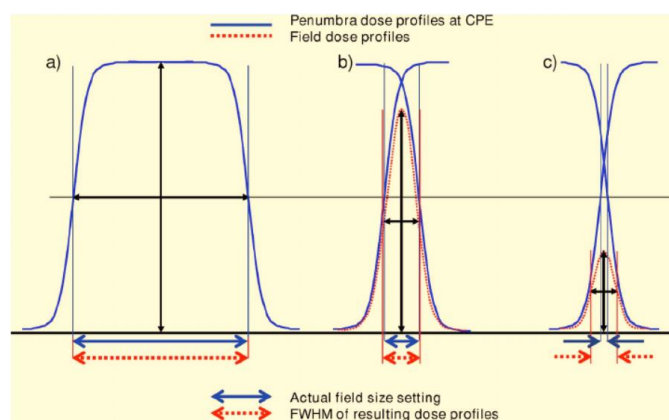
Figure 2.3 The widening of the FWHM from effect of penumbra overlapping compared with the nominal field size by the collimator setting. Figure from Das et al. (1)

The LCPE breaks down together with the occlusion of the primary photon source lead to a sharp drop in the small field output. The high gradient of the beam profile significantly impacts the detector response. In addition, this effect is more pronounced when the density of the material and beam quality increase.

(iii) The size of the detector is large compared to the field size.

The last condition is associated with the size of the detector related to the radiation field width. The signal generated by the detector is proportional to the average absorbed dose over its sensitive volume. If the dimension of the detector is larger compared to the field size, only a portion of the detector volume is exposed to radiation. The detector signal averaged over its volume will underestimate the true value at the field center. In addition, this situation also overestimates the dose beyond the field edge.

Another problem that relates to the detector selection is the perturbation effect of the charged particle fluence. For the small field that exhibits very high dose gradients and lack of LCPE conditions, fluence perturbations become significant. The perturbation effect takes place when the material of the detector is different from the homogenous medium. Then, the averaged electron fluence in the detector is deviated from the actual value in the homogenous medium, leading to the difference in the absorbed dose in the medium that is predicted by the Bragg–Gray cavity theory (5). This effect is also related to the size, shape, and density of the detector. The major perturbations are caused by the difference between the mass density and the medium of the detector. Thus, depending on the detector's mass density, it can cause under or over-respond to the detector signal.

The detector's response is significantly impacted by both volume averaging and perturbation effects. To avoid the above situations, the field size defined by FWHM has to extend at least a distance r_{LCPE} beyond the outer boundaries of the detector (Equation 2.2), which in this case, small field condition is eliminated.

$$FWHM \geq 2r_{LCPE} \pm d \tag{2.2}$$

Where r_{LCPE} is lateral charged particle equilibrium range. the d is the largest dimension of the detector's outer boundary.

2.1.2 Field output factor

Total scatter factor or output factor (OF) is defined as the ratio of absorbed dose to water (D_w) in any clinical field (f_{clin}) for a given beam quality (q_{clin}) to that in a reference field (f_{ref}) with corresponding beam quality (q_{ref}) at a given depth. In board beam, the field output factor

has commonly been approximated by a ratio of detector readings since the perturbation correction factors, and the stopping-power ratios are practical constant with field size at a given photon beam energy, as can be seen in equation 2.3.

$$\text{Output factor} = \frac{D_{w,Q_{clin}}^{f_{clin}}}{D_{w,Q_{ref}}^{f_{ref}}} \approx \frac{M_{w,Q_{clin}}^{f_{clin}}}{M_{w,Q_{ref}}^{f_{ref}}} \tag{2.3}$$

For small fields, the perturbation factors and volume averaging effects vary with detector materials, type, dimension, and field size, which was discussed in 2.1. Therefore, the condition of Equation 2.3 is no longer held. The complete equation of absorbed dose (Equation 2.4) is required to determine the output factors, which stopping power ratio ($s_{w,air}$) and perturbation factor (ρ) need to be defined for each particular small field size.

$$\text{Output factor} = \frac{D_{w,Q_{clin}}^{f_{clin}}}{D_{w,Q_{msr}}^{f_{ref}}} = \frac{M_{w,Q_{clin}}^{f_{clin}} \times (s_{w,air})_{q_{clin}}^{f_{clin}} \times \rho_{q_{clin}}^{f_{clin}}}{M_{w,Q_{ref}}^{f_{ref}} \times (s_{w,air})_{q_{ref}}^{f_{ref}} \times \rho_{q_{ref}}^{f_{ref}}} \tag{2.4}$$

Simpler formalism was proposed by Alfonso *et al.* (6) in 2008 and later applied in TRS 483. The output correction factor ($k_{Q_{clin},Q_{msr}}^{f_{clin},f_{msr}}$) is introduced to correct the differences in the response of a detector in the clinical and reference fields. The detector reading ratio is multiplied by this factor to determine the field output factor as given by Equation 2.5. The author also proposed the term of machine specific reference (msr) field for treatment machines that cannot open a conventional reference field. Therefore, all indices ref are substituted with indices msr.

$$\Omega_{Q_{clin},Q_{msr}}^{f_{clin},f_{msr}} = \frac{M_{w,Q_{clin}}^{f_{clin}}}{M_{w,Q_{msr}}^{f_{msr}}} \times k_{Q_{clin},Q_{msr}}^{f_{clin},f_{msr}} \tag{2.5}$$

The symbol $\Omega_{Q_{clin},Q_{msr}}^{f_{clin},f_{msr}}$ is referred to field output factor that converts the absorbed dose to water from the reference field to the absorbed dose to water of the clinical field.

$$D_{w,Q_{clin}}^{f_{clin}} = D_{w,Q_{msr}}^{f_{msr}} \times \Omega_{Q_{clin},Q_{msr}}^{f_{clin},f_{msr}} \tag{2.6}$$

2.1.3 Determination of field output correction factor

It is clear that this field output factor is defined as a ratio of absorbed doses to water. The symbol $\Omega_{Q_{clin},Q_{msr}}^{f_{clin},f_{msr}}$ emphasize that the field output factor is not identical with traditional OF or

the ratio of detector reading. By combining Equation 2.5 and Equation 2.6 the absorbed dose in the clinical small field can be calculated as follow

$$D_{w,Q_{clin}}^{f_{clin}} = D_{w,Q_{msr}}^{f_{msr}} \times \frac{M_{w,Q_{clin}}^{f_{clin}}}{M_{w,Q_{msr}}^{f_{msr}}} \times k_{Q_{clin},Q_{msr}}^{f_{clin},f_{msr}} \qquad (2.7)$$

Apply this $k_{Q_{clin},Q_{msr}}^{f_{clin},f_{msr}}$ reduces variations and increases consistency of output factor from different detectors and different treatment machines. For relative small field dosimetry, TRS 483 advises to use two or three different types of detectors for a particular measurement as no ideal detector exists.

Following the previous equation, the $k_{Q_{clin},Q_{msr}}^{f_{clin},f_{msr}}$ can be calculated as follow:

$$k_{Q_{clin},Q_{msr}}^{f_{clin},f_{msr}} = \frac{D_{w,Q_{clin}}^{f_{clin}} \big/ M_{Q_{clin}}^{f_{clin}}}{D_{w,Q_{msr}}^{f_{msr}} \big/ M_{Q_{msr}}^{f_{msr}}} \qquad (2.8)$$

Three procedures to drive the $k_{Q_{clin},Q_{msr}}^{f_{clin},f_{msr}}$ are recommended by TRS 483 based on Equation 2.8, which involved measurement and simulation. The first procedure, the reference detector that is nearly water equivalent in terms of density and radiological response, which is considered as perturbation free except for volume averaging such as TLDs, alanine, radiochromic film, and organic scintillators is used to determine $D_{w,Q_{clin}}^{f_{clin}} \big/ D_{w,Q_{msr}}^{f_{msr}}$. The $M_{w,Q_{clin}}^{f_{clin}} \big/ M_{w,Q_{msr}}^{f_{msr}}$ is measured from the observed detector. The second procedure allows the $D_{w,Q_{clin}}^{f_{clin}} \big/ D_{w,Q_{msr}}^{f_{msr}}$ to be determined with the detector with a known $k_{Q_{clin},Q_{msr}}^{f_{clin},f_{msr}}$ when there is no perturbation free detector available. For both procedures, the accuracy of $k_{Q_{clin},Q_{msr}}^{f_{clin},f_{msr}}$ depends on the reference detector.

The last procedure is based on Monte Carlo (MC) simulation. According to Equation 2.8, the reading of the detector is proportional to the absorbed dose in the sensitive volume, then the Equation 2.8 becomes

$$k_{Q_{clin},Q_{msr}}^{f_{clin},f_{msr}} = \frac{D_{w,Q_{clin}}^{f_{clin}} \big/ D_{det,Q_{clin}}^{f_{clin}}}{D_{w,Q_{msr}}^{f_{msr}} \big/ D_{det,Q_{msr}}^{f_{msr}}} \qquad (2.9)$$

These ratios can compute by MC simulation where $D_{det,Q_{clin}}^{f_{clin}} \big/ D_{det,Q_{msr}}^{f_{msr}}$ is the ratio of deposited dose in the sensitive volume of detector and $D_{w,Q_{clin}}^{f_{clin}} \big/ D_{w,Q_{msr}}^{f_{msr}}$ is the ratio of deposited dose in small voxels of water. Then the $k_{Q_{clin},Q_{msr}}^{f_{clin},f_{msr}}$ mostly depend on the modeling of the detector.

2.1.4 Equivalent square field

(i) Equivalent square field size in general

In order to calculate the absorbed dose in the treatment planning system (TPS), a comprehensive set of beam data must be measured as a function of the square field, such as percentage depth dose (PDD), beam profile, and output factor. Since treatment fields in clinical practice are often irregular or rectangular shape, to obtain the above factors for the non-square fields, the concept of an equivalent square field is widely used. The original concept of equivalent squares field refers to the square field which has the same central-axis depth dose distribution as a given non-square field (7). When radiation incident on a homogeneous medium and the LCPE exists, the depth dose at the central axis will be the same, only differences in the scatter radiation will affect the shape of the central axis depth dose (8). Later, the equivalent square field was used with other field size-dependent parameters, such as output factor, and presented in tabular form in the British Journal of Radiology (BJR) supplement 25 (9).

The equivalent field from the BJR table was calculated based on Clarkson's method of scatter function (10). Afterward, Meredith and Neary (11) showed that the scatter function could be represented by an equation involving two arbitrary constants, which could be determined for each set of irradiation conditions such as energy, source to surface distance, and depth. Then, scatter dose in any field can be calculated by an integration involving the scatter function s which is a function of radius r given by

$$s = \frac{SC(r)}{SC(\infty)} = 1 - e^{\lambda r} - \mu \lambda r e^{-\lambda r} \tag{2.10}$$

Where $SC(r)$ is the central axis scatter dose in a circular field of radius r

$SC(\infty)$ is the central axis scatter dose in a field of infinite radius

λ is a scale parameter of dimensions length

μ is a dimensionless shape parameter lying between 0 and 1

In the BJR table, λ=0.26 and μ =0.5 were used to determine the equivalent square fields from a set of rectangular fields (12). The scatter function is explained further in the below sections.

A simpler and most common approximate for equivalent square settings has been developed by Sterling *et al.* (12) They introduced the area over perimeter method, commonly called 4A/P. This expression is mostly applied for rectangular field sizes, where it then becomes

$$E = \frac{X \times Y}{2(X+Y)} \tag{2.11}$$

Where X and Y are the jaw settings, and E is the side of the equivalent square field. Sterling's formula could be applied with minimum error for rectangular fields of moderate elongation factors only. The accuracy of this method decreases when either side of the rectangular field exceeds 20 cm or if the ratio of X/Y exceeds 2 (13).

(ii) Equivalent square field size for small field

In TRS 483 protocol, equivalent square msr fields and equivalent square small fields are introduced. The former is used to determine $TRR_{20,10}$ of msr field for reference dosimetry, whereas the latter is used for selecting the $k_{Q_{clin},Q_{msr}}^{f_{clin},f_{msr}}$ for relative dosimetry.

- Equivalent square msr field

In case of treatment machines that cannot provide the conventional 10×10 cm^2 reference field, hence the need to define a msr field. The msr field is defined as the field that has dimensions as close as possible to the conventional reference field. To avoid the small field condition, the size of the field needs to be larger than a distance of r_{LCPE} beyond the edge of the reference ionization chamber.

The definition of equivalent square msr field is similar to the general equivalent square field. It is specified as the field size that has the same amount of scatter dose on the central axis at the measurement depth as the non-square field (2). In TRS 483, the equivalent square msr field tabulated in Tables 15 and 16 was determined based on the scatter function following Equation 2.11 with μ =0.5 and λ =0.18.

For photon beam with the flattening filter (WFF), the equivalent square mse field can be derived by integration over the scatter function, then the equation 2.10 becomes

$$SC_{field} = \frac{1}{2\pi} \iint_{field\ area} \left(\lambda(1-\mu)\frac{e^{\lambda r}}{r} + \mu\lambda^2 e^{-\lambda r} \right) r dr d\theta \tag{2.11}$$

In flattening fiter free (FFF) beams, the amount of scatter is less than the WFF beams at the same field size due to the bell-shaped beam profile. However, the scatter function of FFF beams is very similar to the WFF beams. The equation 2.11 can also be used for FFF beams. The radial dependence of the lateral beam profile presented by a function F(r) is introduced since the FFF beam exhibits a non-flat lateral beam profile. The equation 2.11 can therefore be written as

$$SC_{field} = \frac{1}{2\pi} \iint_{field\ area} \left(\lambda(1-\mu)\frac{e^{\lambda r}}{r} + \mu\lambda^2 e^{-\lambda r} \right) F(r)\ r dr d\theta \tag{2.12}$$

To determine the equivalent square msr field, its SC_{field} need to be equal to SC_{field} of the non-square field. For example;

$$SC_{10\times5} = SC_{S\times S} \tag{2.13}$$

Where $SC_{10\times5}$ is the scatter component of 10x5 cm^2 rectangular field, and s is the side of equivalent square mrs field. The left-hand side of Equation 2.13 could be calculated by equation 2.11 for WFF beam and Equation 2.12 for FFF beam. The the $SC_{S\times S}$ can be obtained by solving the equation.

- Equivalent square small field (S_{clin})

While the equivalent square msr field is the result of equating the scatter component (SC) of the non-square field and the equivalent square field, the determination of the S_{clin} is very different due to the absence of scatter.

For the small field where the collimator devices open a very small aperture, the scattered radiation from the primary collimator, flattening filter, and other materials in the linac head is shielded by those collimators. This results in the reduction of low energy photons fluence reaching the central axis of the small field. Hence, the S_{clin} is the field that exhibits the same detector perturbation factor as the rectangular or circular small field when both of head scatter and phantom scatter is absence.

In TRS 483, the $k^{f_{clin},f_{msr}}_{Q_{clin},Q_{msr}}$ for small fields are tabulated as a function of S_{clin}. For non-square fields, a method is provided to determine S_{clin} for which the $k^{f_{clin},f_{msr}}_{Q_{clin},Q_{msr}}$ are the same. This method was proposed by Cranmer-Sargison *et al.* (3), who introduced an effective field size defined by the radiation field width for small field dosimetry. They found the consistency of the output ratios among the five linear accelerators when reported with the effective field size for field < 1x1 cm^2. Later, the effective field size was adopted by TRS 483 as S_{clin} that defined as

$$S_{clin} = \sqrt{A \times B} \tag{2.14}$$

Where A and B correspond to the in-plane and crosss-plane dosimetric field width (FWHM), respectively. The S_{clin} method simply uses the area of the non-square small field equates with square small fields. The reason behind this method is based on the independence of the phantom scatter factors on the collimation and linac type when the field size is smaller than 4x4 cm^2. For a small field where the phantom scatter factor depend only on measurement depth and the field area (14), using the area of the field size is suitable to compare dosimetric quantities of a

small field among different linacs or different collimator devices (jaws, MLCs and cones) (3). Thus, the 4x4 cm^2 field size is taken as the borderline field between the equivalent square field size for the board beam method and the small field size (S_{clin}) method.

The output factors in a large field are stable for a sub-millimeter size difference between nominal field size and radiation field size. In contrast to the small field output factor that will significantly change when this difference exists. In addition, there can be a difference between the geometric field size or the actual opening aperture by jaws and/or MLCs and the nominal field size as set on the linac console. This is due to collimator calibration and the position accuracy of the collimator system (15). Thus, the use of S_{clin} with $k_{Q_{clin},Q_{msr}}^{f_{clin},f_{msr}}$ could provide consistency and standardize across measurements *across* all *linacs*.

The length and width of the dosimetric field are adequate to represent the S_{clin} if the field is not too elongated or when A/B is in between 0.7-1.4. Outside of this range, a larger uncertainty on the $k_{Q_{clin},Q_{msr}}^{f_{clin},f_{msr}}$ should be considered.

2.1.5 Elongated small field in Treatment Planning System (TPS)

Currently, the available TPS at the division of Radiation Oncology, King Chulalongkorn Memorial Hospital, is Eclipse (Varian Treatment Planning System, Varian Inc., Palo, Alto, USA). The commissioning beam data measurements have been performed since the installation of the treatment machine. For beam data acquisition, there are several beam characteristics that have to be measured, such as percentage depth doses (PDDs), beam profiles, and field output factors. Output factors are typically measured at a depth of 10 cm and are displayed as a ratio of dose at depth for each field size with respect to the dose at the reference field size of 10x10 cm^2. The anisotropic analytical algorithm (AAA) and Acuros XB are available in the Eclipse TPS for the calculation of absorbed dose. Output factors required for those algorithms are displayed in Table 2.1. The side of the field is ranged from *2* cm to 40 cm, leading to a total of 64 field sizes. Due to the complexity of small field dosimetry, no measurement data is required for field sizes below 2x2 cm^2. Thus, the TPS will interpolate the output factor from the existing data for fields that were not measured.

Table 2.1 Field sizes required for output factor

		Field size X (cm)								
		2	3	5	7	10	15	20	30	40
Field size Y (cm)	2									
	3									
	5									
	7									
	10									
	15									
	20									
	30									
	40									

Another TPS which requires the output factors of long narrow fields for the commissioning process is RayStation (RaySearch Medical Laboratories AB, Stockholm, Sweden) with the collapsed cone algorithm. The elongated field sizes required for this TPS are 40x5, 5x40, 20x5, 5x20 cm^2. However, these field sizes are not necessary for Monaco TPS (Elekta CMS, Maryland Heights, MO, USA) whose dose computation of photon is based on a Monte Carlo (MC) algorithm.

2.1.6 Monte Carlo simulation

The Monte Carlo (MC) simulation is a statistical method for performing numerical integrations and solving mathematical problems. The MC technique was first developed at the end of the second world war to calculate radiation transport for nuclear weapons (16).

MC methods use a random number generator and probability statistics to obtain parameter values for solving the problem for a single event. The results are calculated as average values. Because the result is an average, it is associated with a standard deviation that represents the uncertainty. The uncertainty can be reduced and increased the accuracy of the results by using many events (17). The MC method can help solve complex problems where analytical approaches cannot perform when changes in the relationship between parameters, or the introduction of a new parameter, may produce difficulty in finding a new analytical solution.

The interaction of radiation with matter is probabilistic, and the physics of different radiation interactions with matter and their probability distributions are well understood. Therefore, the MC method can simulate the scenario of the radiation transport to calculate the deposited

dose (18) when the measurement is not possible or somewhat challenging. It has been proven that MC is an effective tool in overcoming the challenges of small field dosimetry. Many authors published the $k_{Q_{clin},Q_{msr}}^{f_{clin},f_{msr}}$ for several detectors calculated by MC simulation (19-23).

The MC method simulates the tracks of individual particles through the volume of interest for radiation transport problems. The particle may interact with the matter through its interaction, such as the photoelectric effect, Compton scattering, and pair production. The program keeps track of those particles of interest for a large number of histories to calculate the reliable information in terms of averaged quantities (17).

At present, the wide variety of MC codes that are available, those that are most frequently used for modeling radiotherapy beams is ETRAN/ITS, EGS4, EGSnrc, MCNP4, PENELOPE, and, most recently, GEANT3 and GEANT4 (24). The focus of this thesis is on EGSnrc, which is briefly explained below.

(i) EGSnrc Monte Carlo code

Electron Gamma Shower (EGS) is a general purpose MC code package to simulate the transport of electrons, photons, and positrons with energies in the range of a 1 keV to 10 GeV through matter. EGSnrc is an improved version of EGS4, which was developed initially at the Stanford linear accelerator center in 1970. Later, the modifications introduced to EGS4 by the National Research Council of Canada (NRC), improved its use in radiotherapy modeling (25-28).

- BEAMnrc is an EGSnrc code for modeling the radiotherapy sources or linac treatment head. This code provides the user with the various geometrical shape or component modules for the model a full linac. Each component module is designed to represent the component in real linac, such as the primary collimator, flattening filter, ionization chamber, and the jaws. To create the particle transport in the treatment head, the full linac model or phase-space file can be used as an input for BEAMnrc. This process creates a radiation beam that reflects the dosimetric characteristics of that generated by a real treatment head. After the BEAMnrc simulation, a phase-space file is created as a primary output. This file contains information on all particles such as direction, type, and energy crossing the XY-plane along the Z-axis.

- DOSXYZnrc code package is designed to calculate the dose distributions inside the phantom with a rectilinear voxel. Each voxel can be assigned with a physical density that represents the actual material. The dimension of the voxel is variable in three directions. This code also provides the calculation of absorbed dose in CT images.

- Egs_chamber is an EGSnrc user code developed for modeling radiotherapy dosimeters. This code also uses a source input such as full BEAMnrc linacs or the phase-space file. The egs_chamber user code is used to assess a detector's dose corrections factors. It allows the user to model the detector with different geometries and is not limited to rectilinear shape.

2.1.7 An overview of detectors for relative small field dosimetry used in this work

Relative dosimetry refers to the ratio of absorbed dose at a point to the dose at some reference point. This includes the determination of dosimetric quantities such as central axis depth dose curves, tissue maximum ratios, tissue phantom ratios, beam profiles, and field output factors as a function of field size. Relative dosimetry measurements are used as entry data in TPS during commissioning after installation of the linear accelerator machine. A major problem in small field dosimetry is the perturbation of the radiation field due to the presence of a non-water materials detector and the volume averaging effect caused by the finite size of the detector's active volume. The necessary properties of an ideal detector for a small field are water equivalent, small active volume, energy independent, and dose rate independent (2). Various detectors have been available on the market for small field dosimetry. These include cylindrical ionization chambers, diodes, synthetic diamonds, radiochromic film, plastic scintillators, MOSFETS, gel dosimeters and more. However, none of these detectors has all the aforementioned properties. Thus, no ideal detector exists for a small field.

The objective of this dissertation is to determine the field output correction factors for elongated small field. For the scope of this work, we have selected the ionization chamber CC01 from IBA, Exadin W2 plastic scintillator detector (PSD) from Standard Imaging, and the diode silicon EDGE detector from Sun Nuclear based on their suitability to the investigated situation. The ionization chamber IBA CC01 is selected due to its suitable dosimetric characteristics such as energy independence, good linearity, and reproducibility. This chamber also has a small correction factor for field output factor measurement down to 0.6x0.6 cm^2 in S_{clin}. The Standard imaging Exadin W2 plastic scintillator detector (PSD) is good candidate for small field dosimetry because it expresses the tissue equivalence characteristics, density similar to water, stable photon energy response, and very small dimension. Overall the PSD exhibits a small perturbation correction factor with the field output correction factor equal to unity for every small field size. The high sensitivity of Edge detector permits their construction with a very small size, an appropriate characteristic for small field dosimetry. An overview of small field dosimeters is presented in the following sections.

(i) Cylindrical ionization chambers

Ion chambers are the simplest type of all gas-filled radiation detectors. The term "ionization chamber" refers to those detectors which collect all the charges generated by direct ionization inside the gas using the influence of an electric field (29). These chambers come in various sizes and shapes, depending on their application but there are generally four common types of ionization chambers for medical physics application (30); Free-air chambers for air kerma measurement at primary standard, Cylindrical or thimble ionization chambers for reference and field dosimetry, Parallel-plate chamber for lower photon energy and electron beam dosimetry, and transmission chamber for monitoring the output of the radiotherapy machine when the beams pass through the chamber. This section focuses on the cylindrical ionization chambers only since this chamber is well-known as the gold standard tool in clinical dosimetry.

Typically, a cylindrical ionization chamber is an air-filled cavity that has the collecting electrode in the center of the cavity and is surrounded by a conductive outer wall, as presented in Figure 2.4. The chamber wall is often made of an air equivalent material such as graphite or polymethylmethacrylate (PMMA). The central electrode is usually made of aluminum, graphite, or steel. The insulator is placed between the chamber wall and the central electrode to reduce the leakage current when a polarizing voltage is applied to the chamber. To further minimize chamber leakage, a guard electrode is usually placed next to the air cavity, which is a cylindrical shape conductor that covers the insulator and contact with the central electrode.
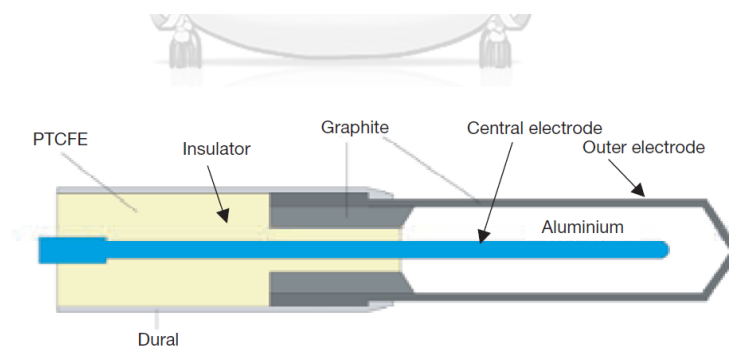
Figure 2.4 The schematic of a cylindrical ionization chamber. Figure from E.B.Podgorsak, Radiation Oncology Physics: A handbook for teachers and students.

The operating principle is based on a collection of all the charges created by direct ionization within the air. A polarizing voltage, typically 200 V to 400 V depending on the chamber type, is applied between the outer wall and central electrode to create an electric field. When the chamber is irradiated, the interaction of photons with the chamber walls produce electrons that traverse the air cavity, causing ionization of the air. The created ion pairs (electron and positively

charged atoms) inside the cavity are attracted to the electrode under the influence of the electric field. Then, depending on the polarity of the applied polarizing voltage, the ions of one sign are collected by the central electrode, causing an electric current which is measured by an electrometer. The measured current is simply proportional to the rate of formation of charge and is proportional to the absorbed dose in the air volume of the chamber cavity.

The most popular cylindrical (thimble) ionization chamber is the chamber with an active volume of 0.6 cm^3 designed by Farmer and available from several vendors for reference dosimetry like beam calibration. Some corrections are needed for the cylindrical ionization chambers when used for beam calibration, such as ion recombination correction for the recombination of the electron positive charge atom before reaching the electrode and temperature and pressure correction for the change in the mass of air inside the cavity when the ambient temperature and pressure are changed. However, for the relative dosimetry, including percentage depth dose, beam profile, and field output factor, these corrections can be excluded from dose calculation since they are practically constant with field size for given beam energy.

For small field dosimetry that requires detectors with high spatial resolution, cylindrical chambers with active volumes between 0.1 and 1 cm^3 are produced by various manufacturers. The small size of the volume can reduce the volume averaging effect but can lead to a low signal-to-noise ratio (SNR) since it produces very small ionization currents. To improve the SNR, delivering a large MU to the chamber is recommended. The central electrode of some small cylindrical chamber is constructed from a high atomic number material (e.g., steel) in order to increase the signal from their small cavity.

(ii) Plastic scintillator detector

The plastic scintillation detector (PSD) showed excellent dosimetric characteristics for small field dosimetry owing to its small dimensions and nearly water equivalence. The principle of the PSD is based on the property of scintillating materials (inorganic and organic materials) that produce light when they absorb ionizing radiation. This property is related to luminescence which is defined as a rapid emission of light from the excitation of the materials (31). For an inorganic material, the luminescence phenomena are explained by using the energy band model. In comparison, the luminescence of an organic material arises from transitions in the energy levels of a single molecule.

The process of luminescence for inorganic materials consists of three steps: (1) the creation of electron-hole pair; (2) the stimulation causes an escape of electrons and holes; (3) electron-hole recombination under emission of luminescence. Figure 2.5 illustrates the energy band diagram of luminescence processes in an inorganic crystal.

When radiation interacts with the crystal, the electron is excited from the valence band to the conduction band. The lack of electrons creates a hole in the valence band. The electron then moves toward the conduction band and becomes trapped in the forbidden band. Similarly, the hole migrates through the valence band and becomes trapped at a recombination center. During this process, the electron trap can be stimulated by using thermal or optical, depending on what makes the electron escape from the traps. This thermal and optical trap can be used for optically-stimulated luminescence (OSL) and thermoluminescence (TL) dosimetry. Finally, the electron recombines with a hole at the recombination center and emits a light photon.
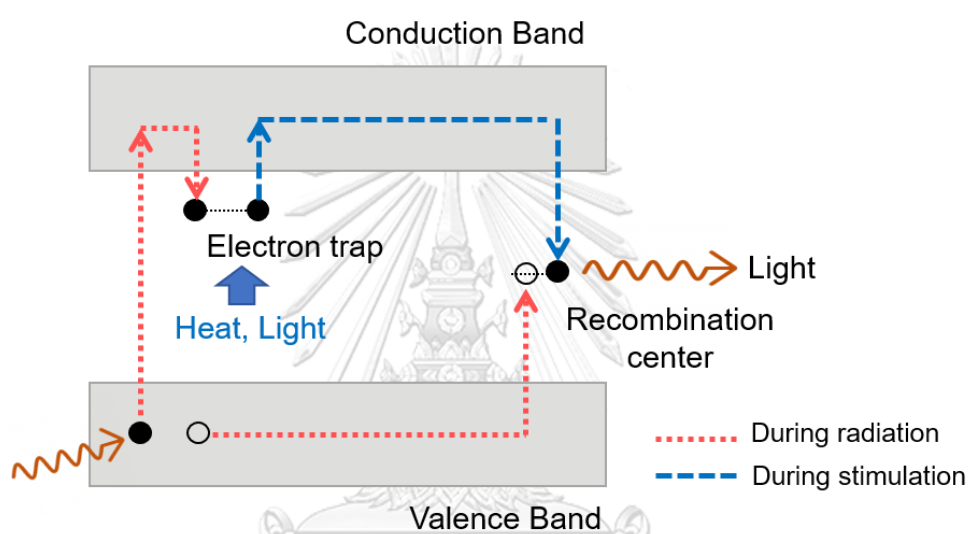
Figure 2.5 The energy band diagram of luminescence processes in the inorganic crystal.

For the PSD that is made for organic material such as polystyrene, the luminescence phenomena is based on transitions in the energy level structure of a single molecule (29). On a molecular level, the excitation process that produces luminescence is occurred by π-electrons structure. Figure 2.6 presents the energy of an organic molecule with a π-electrons structure. The singlet state and triplet state are presented with a series of S and T, respectively. When the organic material is irradiated, the molecule is excited to a higher energy band. If the molecule undergoes the singlet state, it will quickly (on the order of picoseconds) de-excited to the ground stated (S_0) and prompt emit visible light. This phenomenon is called "Fluorescence" which is the main process of a singlet–singlet transition from S_{10} to S_0. If the molecule receives excess energy ($\geq S_{11}$) it will quickly lose the energy by vibrational relaxation and transition to S_{10}. Therefore, the net effect of the fluorescence process is produced on the S_{10} state. If the electron transits from the singlet band to the triplet state first level (T_1), the electron de-excites from T_1 to S_1 and will produce delayed light emission (10^{-6} s or longer) characterized as "Phosphorescence". Finally, the light produced

by organic and inorganic material is detected by a photodiode or photomultiplier tube that produces a current proportional to the incident light.
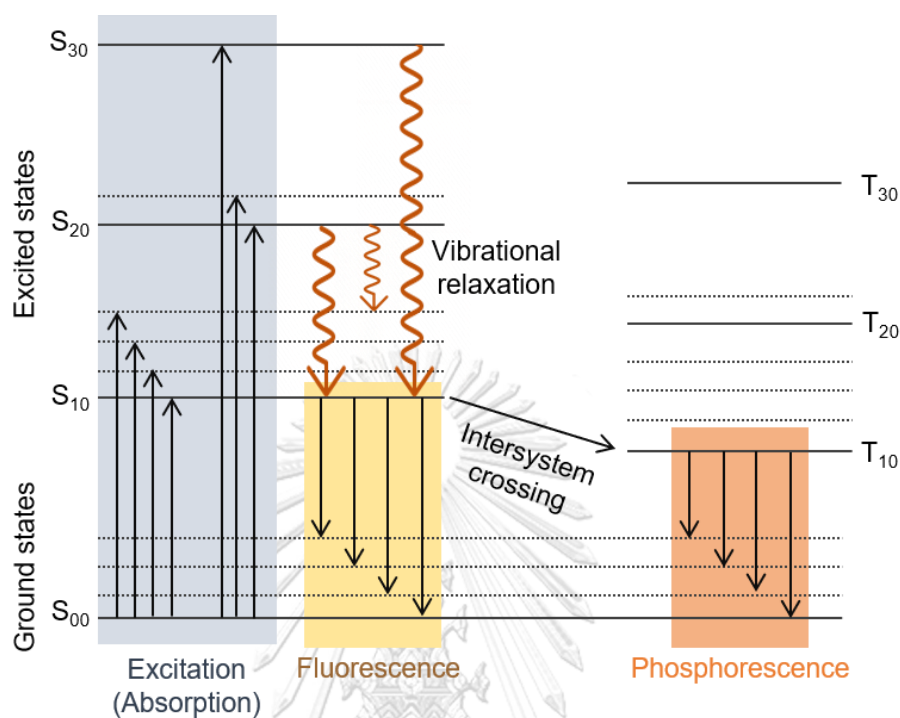
Figure 2.6 Energy levels diagram with the π-electron structure of an organic molecule

Although scintillation dosimetry is one of the oldest techniques on record, the application of the PSD in clinical dosimetry is still being developed. Currently, only two detectors; The Exradin W1 PSD and W2 PSD from one manufacturer (Standard Imaging, Middleton, WI) available on the market. Both W1 and W2 PSD are similar, differing only in the length of active volume (W1 is 3 mm length and W2 is 1 mm length).

Both PSDs are made from polystyrene and enclosed in a black ABS jacket to shield them from external light, as presented in Figure 2.7. When exposed to radiation, the molecule of the polystyrene is excited. The produced light in the active volume is transferred through an optical fiber to a photodiode in the electrometer.

.
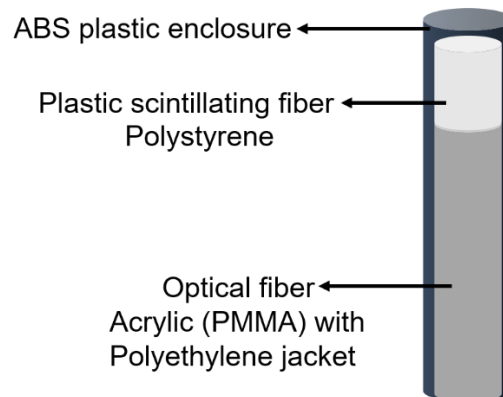
Figure 2.7 Schematic view of the Exradin W1 plastic scintillator detector

The main disadvantage of the PSD is the Čerenkov radiation or light produced by the optic fiber that guides the light, results in an unwanted light signal and interferes with a dose measurement. The Čerenkov radiation is generated when the charged particles pass through a transparent medium at a velocity greater than light in the same medium (31). Thus, the Čerenkov light needs to be subtracted from the actual scintillating light. Many correction methods have been implemented. The most proven successful methods are spectral filtration and the use of hollow-core fibers (32). APPENDIX II further describes the calibration process of the Čerenkov light for the Exradin W2 PSD.

(iii) Silicon diode detector

A silicon (Si) diode dosimeter is a semiconductor device typically consisting of a p-n junction. This junction is produced by doping a pure Si substrate to become either an n-type or p-type material. The n-type material is created when the donor impurities (P, As) are added to the silicon. These elements have five valence bonds, while silicon has four valence bonds. The free electrons are produced from the extra valence bond of the impurities. In contrast, the p-type region is created when the electron is deficient. When the acceptor impurity (B) that has one lower valence electron than the surrounding silicon atoms is substituted, then the hole is formed. The diode can be n-type or p-type, depending on the majority of the carriers. If the majority of carriers are holes, the diode is called p-type. Similarly, if silicon has an excess of an electron, it is called n-type. The interface between the p-type and n-type material is referred to as the depletion region created from the diffusion of holes from the p-region and electrons from the n-region. The diffusion of charge carriers also produces the electric field or built-in potential inside the diode, which prevents the diffusion further of electrons and holes (Figure 2.8).
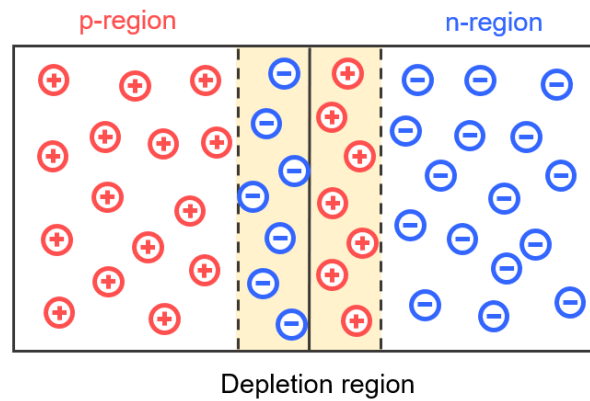
Figure 2.8 p-n junction diode

When ionizing radiation incident on a silicon diode with the band structure shown in Figure 2.9, the electron-hole pairs are created. The minority carriers (electrons on the p-region and holes in the n-region) are diffused toward the p-n junction, where they will be collected by the electric field present in the depletion region.
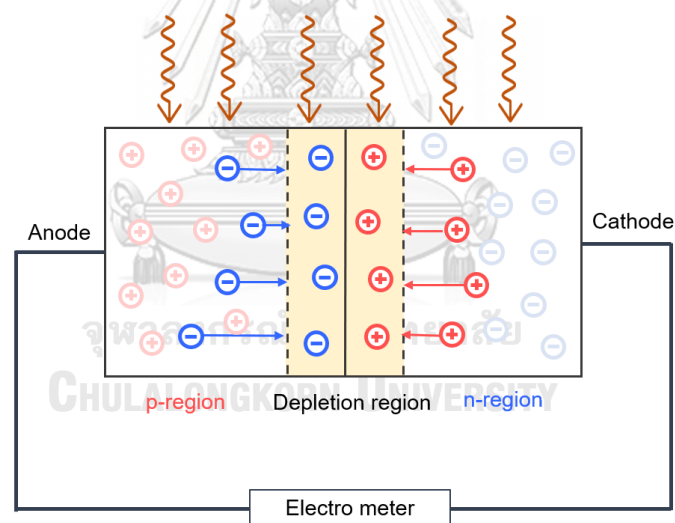
Figure 2.9 The diagram of a p-n junction in silicon diode as a radiation detector

The main advantage of the diode detector is its higher sensitivity. Since the density of the silicon is approximately 1000 times greater than gas, the probability of radiation interactions is increased. Thus, the sensitivity of the diode is much more than the ion chambers with the same volume. Thus, the diode detectors can be constructed very small, resulting in a high spatial resolution with a small volume averaging effect. The main disadvantage is its over-response to low energy photons. However, the absence of scatter radiation in the small field makes this over-response effect rather low. Two common types of diode detectors are commercially available: an

unshielded diode and a shielded diode with a tungsten or brass filter to decrease the fluence of low energy photons.

2.2 Literature review

In this study, we have selected three different types of detectors which the $k_{Q_{clin},Q_{msr}}^{f_{clin},f_{msr}}$ were intensively investigated by previous studies; the ionization chamber (IBA CC01), the shielded diode detector (Sun Nuclear EDGE), and the plastic scintillator detector (Standard imaging Exradin W2). Later, the $k_{Q_{clin},Q_{msr}}^{f_{clin},f_{msr}}$ from those studies were taken by TRS 483 to create the comprehensive tabulated $k_{Q_{clin},Q_{msr}}^{f_{clin},f_{msr}}$ for a wide range of detectors. The $k_{Q_{clin},Q_{msr}}^{f_{clin},f_{msr}}$ for each detector was determined by fitting the entire set of data for all field sizes (experimental and Monte Carlo) with S_{clin}. Figure 2.11 presents the $k_{Q_{clin},Q_{msr}}^{f_{clin},f_{msr}}$ of three detectors as a function of S_{clin}.
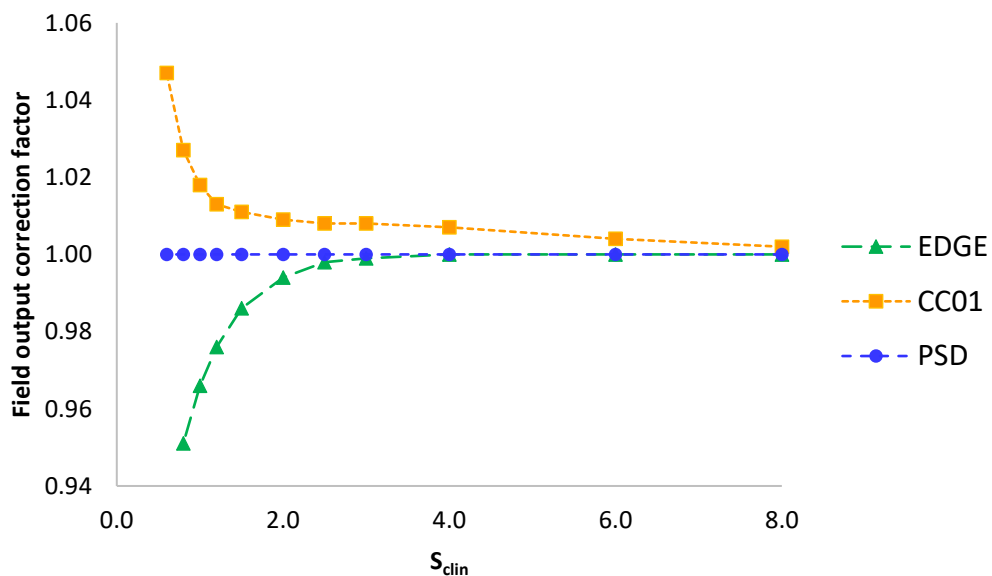
Figure 2.11 Field output correction factor ($k_{Q_{clin},Q_{msr}}^{f_{clin},f_{msr}}$) as a function of S_{clin} at a depth of 10 cm, for a reference field size 10x10 cm² in the water of 6 MV photon beams.

For IBA CC01, the $k_{Q_{clin},Q_{msr}}^{f_{clin},f_{msr}}$ was increased as the field sizes decreased with the $k_{Q_{clin},Q_{msr}}^{f_{clin},f_{msr}}$ up to 4.7% for S_{clin} of 0.6x0.6 cm². The large sensitive volume of the chamber causes the volume averaging effect in the small field, leading to the underestimation of the signal when compared to water (19, 33). Therefore the $k_{Q_{clin},Q_{msr}}^{f_{clin},f_{msr}}$ was more than 1%. Although the IBA CC01 clearly represents the volume averaging effect, it is the only ion chamber that TRS 483 provides

the $k_{Q_{clin},Q_{msr}}^{f_{clin},f_{msr}}$ down to 0.6x0.6 cm^2 (see Table 26 in TRS 483). The central electrode of the IBA CC01 is constructed with steel to increase the signal from their small cavity. The under response of this ion chamber is compensated by an over response due to the presence of the steel electrode. In addition, the output ratio measured by the IBA CC01 at 0.6x0.6 cm^2 was within 2% when compared with the output ratio measured by small perturbation detector like alanine (34).

In contrast, the $k_{Q_{clin},Q_{msr}}^{f_{clin},f_{msr}}$ of Sun nuclear EDGE detector decreased as the field sizes decreased. The explanation of the over response of the detectors in a small field is based on the impact of high density silicon on the LCPE effect (19). Typically, for board beam, the LCPE is presented in both the sensitive volume made of silicon detector and in the same volume of water. When the beam becomes small, the LCPE is greater reduced in water than in silicon because of the longer range of electrons in water. The LCPE remained in the silicon owing to the high-density leading to a short distance of electrons when traveling through the materials. Thus, the over-response of the EDHE detectors is noticed for small field sizes. Thus, the correction factor was smaller than unity (19, 35).

The plastic scintillator detector shows the $k_{Q_{clin},Q_{msr}}^{f_{clin},f_{msr}}$ equal to unity for every field size down to 0.5 cm. This detector is a suitable candidate for small field dosimetry because its density is close to the values of water. They are considered perturbation free detectors except for volume averaging. A good agreement, within 1.5%, was reported by Morin *et al.* (36) when comparing the output factor measured by PSD with the MC simulation for fields with diameters from 0.5 to 6 cm.

For relative dosimetry, the $k_{Q_{clin},Q_{msr}}^{f_{clin},f_{msr}}$ of various detectors were intensively investigated for small field size. However, the majority of previous studies have focused on square fields (19, 21, 22), and very few include measurements of elongated fields. To the best of our knowledge, only two studies that reported the $k_{Q_{clin},Q_{msr}}^{f_{clin},f_{msr}}$ in elongated small field; Francescon *et al.* (23) and Qin *et al.* (37). The former studied the $k_{Q_{clin},Q_{msr}}^{f_{clin},f_{msr}}$ using the Monte Carlo simulation whereas the latter using the measurement to determine the $k_{Q_{clin},Q_{msr}}^{f_{clin},f_{msr}}$.

Francescon *et al.* (23) determined a complete set of $k_{Q_{clin},Q_{msr}}^{f_{clin},f_{msr}}$ for PTW 60012, Sun Nuclear EDGE diode, microchambers PTW PinPoint, Exradin A16, and PTW microLion by using the Monte Carlo simulation. Two different linear accelerators were simulated; Primus^{TM} (Siemens, Erlangen, Germany) and Synergy^{VR} (Elekta,Stockholm, Sweden). For rectangular small fields, the nominal side of the field ranged between 0.5 and 3 cm, in X and Y directions, a total of 36 field sizes. The results showed that the $k_{Q_{clin},Q_{msr}}^{f_{clin},f_{msr}}$ depend on which side of the field defines the X (cross-plane) and Y (in-plane) aperture of the jaw. This is due to the difference in the penumbra between X and Y profiles that affect the calculated dose in the sensitive volume of the detectors. This effect was more pronounced for the Synergy when compared to the Primus, owing to the farther distances between the jaws and the primary source. Thus, large differences between X and

Y profile shapes were noticed for the Synergy machine at a very small field (0.5x0.5 cm^2). The difference in X and Y profiles on the $k_{Q_{clin},Q_{msr}}^{f_{clin},f_{msr}}$ was found to be more pronounced for microchambers than for diodes, due to the larger sensitive volume of the ion chamber.

Qin *et al.* (37) investigated small field output factors for 6 FFF MV photon beams on a Varian EDGE linac for 16 field sizes with X and Y jaw combinations, each set to 0.5, 1, 1.5, and 2 cm. Five different detectors were included in this study: IBA CC01 ionization chamber, PTW SFD, Sun Nuclear EDGE diode, Exradin W1 scintillator detector, and Gafchromic EBT3 film. The output factors (OF) of elongated field sizes were measured and the collimator exchange effect was calculated using the following formula.

$$CE = \frac{OF\ (X,Y)}{OF\ (Y,X)} - 1$$ (2.15)

Where X and Y were the respective X and Y jaw settings. Figure 2.10 presents the correlations between the jaw ratio and the CE effect. The averaged CE effect was 4.2% ± 4.5% across all detectors and field sizes. In addition, Qin's study also reported the decrease of the output factors when opening a smaller Y jaw. For example, the field size (X x Y) of 1×0.5 cm^2 gave a smaller output factor of 0.53 when compared to the output factor of 0.58 for the opposite field size of 0.5x1 cm^2. The explanation is based on the size of the upper Y jaw that is closer to the monitor chamber. When opening a smaller Y jaw, the backscatter was increased into the monitor chamber. Thus, The MU delivered to the detector was decreased and produced a smaller output factor.

The correlation between the CE effect and the elongation of the field represented by the jaw ratio was noticed for all detectors. The greater the CE effect was found with more elongation of the field. A similar correlation coefficient between 0.88 to 0.90 was reported across all detectors. It was noticed that the largest CE effect belonged to fields with either X and Y jaw set at 0.5 cm. This could be due to the primary source occlusion effect when the side of the field is very small.
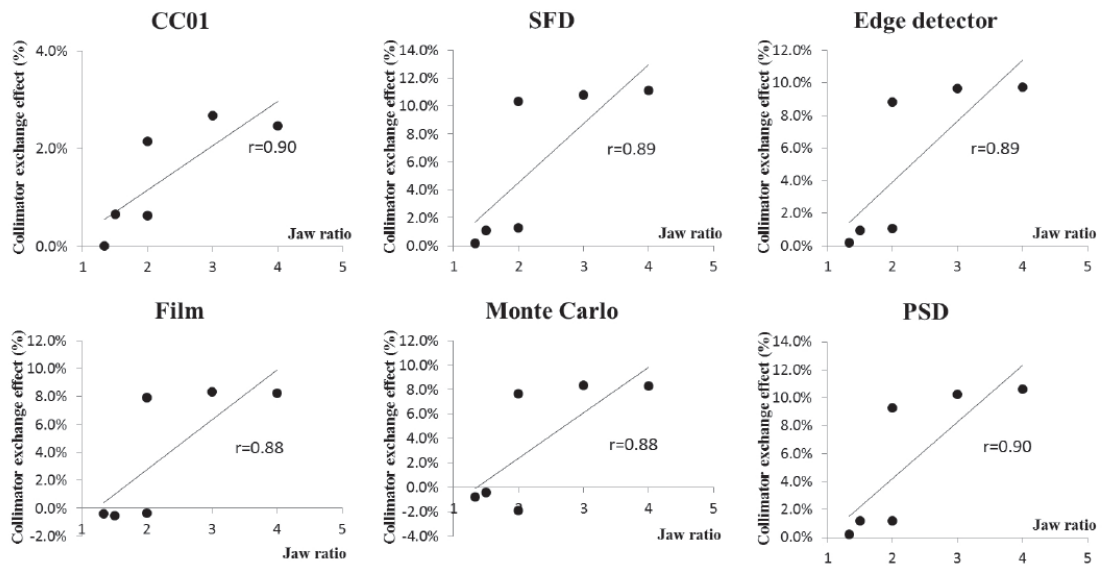
Figure 2.10 The CE effect plotted against jaw ratios (Y/X). The correlation coefficient (r) was calculated for each detector. Figure from Qin et al. 2016).

From Francescon and Qin study, we can conclude that the $k_{Q_{clin},Q_{msr}}^{f_{clin},f_{msr}}$ of elongated small fields depend on the shape of cross-plane and in-plane beam profiles that influence by the X and Y jaw, also the size of the sensitive volume of the detector. In addition, the difference in cross-plane and in-plane length of the elongated field.

จุฬาลงกรณ์มหาวิทยาลัย

CHULALONGKORN UNIVERSITY

CHAPTER 3

MOTIVATION

New international dosimetry protocol for small fields TRS 483 has provided guidelines on the calibration of msr fields and the determination of $\Omega_{Q_{clin},Q_{msr}}^{f_{clin},f_{msr}}$ in small static fields. However, the clinical practice of this new protocol cannot be applicable for dosimetry in elongating small field sizes that are used as entry data in beam commissioning of the treatment planning system since the equivalent square small field size for these field sizes cannot be specified. There is thus a need for the determination of the field output correction factors for elongated small fields.

จุฬาลงกรณ์มหาวิทยาลัย
CHULALONGKORN UNIVERSITY

CHAPTER 4

RESEARCH METHODOLOGY

4.1 Research question

What is the field output correction factor for elongated small field?

4.2 Research objective

To determine the field output correction factor for elongated small field

4.3 Research design

Observational descriptive study

4.4 Research design model

This research design was divided into two parts; The Monte Carlo simulation and the field output factor measurement. The $k^{f_{clin},f_{msr}}_{Q_{clin},Q_{msr}}$ of IBA CC01, Sun Nuclear EDGE detector, and Exradin W2 PSD were calculated by using the Monte Carlo simulation. To confirm the applicable of our calculated $k^{f_{clin},f_{msr}}_{Q_{clin},Q_{msr}}$, the measurement of field output factors was carried out by using identical detectors. Finally, both $k^{f_{clin},f_{msr}}_{Q_{clin},Q_{msr}}$ from TRS 483 and our study were applied with the measured field output factor.
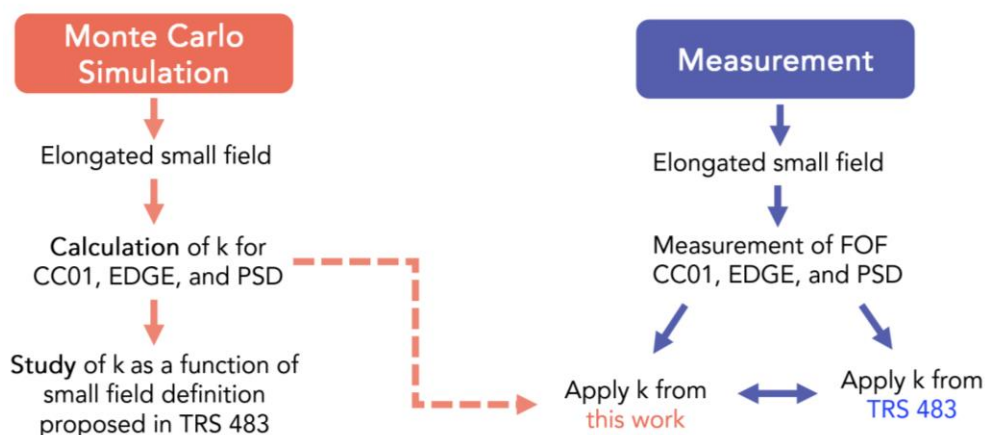
Figure 4.1 Research design model of this thesis

4.5 Conceptual framework

Equivalent square small field size is affected by several factors as described in Figure 4.2
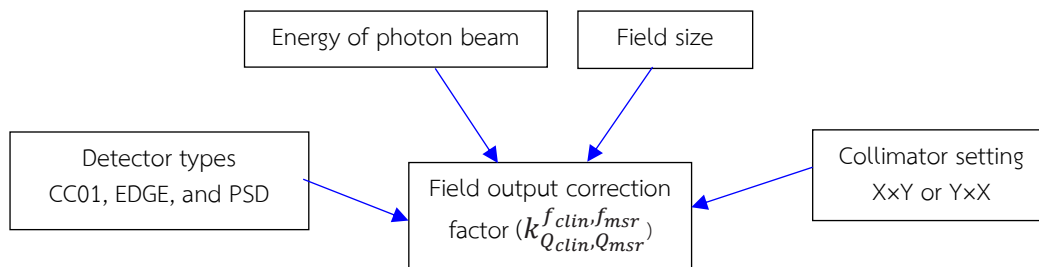
Figure 4.2 Conceptual framework

4.6 Expected benefit

- Improve the accuracy in elongated small field output factor
- Improve the accuracy of patient treatment in advanced radiation therapy technique

4.7 Variable measurement

- Independent variable: detectors, MC parameters, and field sizes
- Dependent variable: field output factor

4.8 Data collection

The calculated absorbed dose in water and in the sensitive volume of detectors was collected from the Monte Carlo study. The measured field output factors were collected from the experimental study.

4.9 Data analysis

The field output correction factor of detectors was evaluated as a function of field sizes.

4.10 Outcome measurement

The correction factors of IBA CC01 ionization chamber, Sun nuclear EDGE detector, and Standard Imaing Exradin W2 plastic scintillator detector for elongated small fields.

4.11 Statistical analysis

Descriptive statistics were used to describe or summarize the characteristics of data, such as average, standard deviation, and percentage difference.

4.12 Ethical consideration

This study has received an exemption determination from the Institutional Review Board of the Faculty of Medicine, Chulalongkorn University, Bangkok, Thailand.

CHAPTER 5

MATERIALS AND METHODS

5.1 Materials

5.1.1 Linear Accelerator

Varian TrueBeam[TM] linear accelerator (Varian Medical System, Palo Alto, CA, USA) is displayed in Figure 5.1. This linear accelerator provides a variety of radiation delivery techniques, including 3D-CRT, IMRT, VMAT, SRS, SRT, and SBRT. The system consists of a flattened and unflatten photon beam of 6 MV and 10 MV energy. The electron beam is available in 6, 9, 12, 15, 18, and 22 MeV. The Varian TrueBeam[TM] is equipped with a Millenium 120 leaf MLC that can shape the beam into different shapes and sizes to match the shape of the tumor. In this study, the flattened beam of 6 MV was used, and the field sizes were defined by the jaw system.

Figure 5.1 Varian TrueBeam[TM] linear accelerator

5.1.2 Detectors

Three detectors were used in this study; IBA CC01 (IBA Dosimetry, Nuremberg, Germany) ionization chamber, Exradin W2 plastic scintillator detector (PSD) (Standard Imaging, Middleton, USA) and Sun nuclear EDGE (Sun Nuclear Corporation, Melbourne, FL) shielded diode detector, and which are shown in Figure 5.2. The details of the detectors are explained further below.

a.   b.   c.
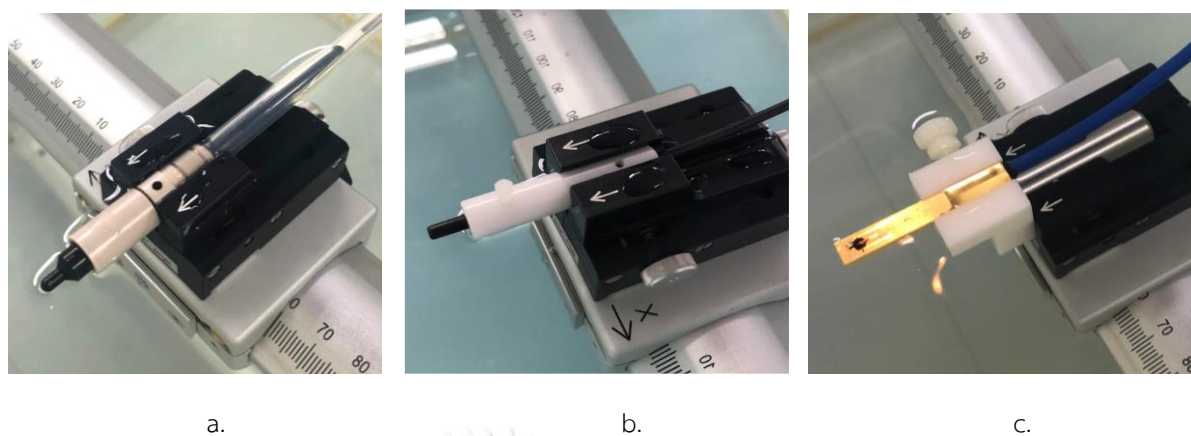
Figure 5.2 (a.) IBA CC01 (b.) Exradin W2 PSD (c.) Sun nuclear EDGE detector

(i) IBA CC01 ionization chamber

The IBA CC01 is a cylindrical ionization chamber with an active volume of 0.01 cm³. The inner electrode is made from steel with a diameter and length of 0.35 mm and 0.28 mm. The detector wall is made from Shonka C-552 plastic with a 2 mm inner diameter and 0.5 mm wall thickness. The chamber specification is summarized in Table 5.1.

Table 5.1 Characteristics of IBA CC01

Detector	Cavity volume (mm³)	Cavity length (mm)	Wall material	Wall thickness (g/cm³)	Central electrode material
IBA CC01	10	3.6	C-552	0.088	Steel

(ii) Exradin W2 plastic scintillator detector (PSD)

The detail of Exradin W2 PSD is listed in Table 5.2. The detector consists of three components: (1) a scintillating plastic material that generates visible light when exposed to radiation, (2) an optical fiber that transfers the light, and (3) an electrometer that changes the light into an electronic signal. The sensitive volume of the detector is 1 mm in diameter by 1 mm long (0.0008 cm³). The detectors are almost water equivalent in terms of electron density and atomic composition (ρ = 1.05 g/cm³), and the perturbation correction in small fields is

close to unity (2). The main complication in the use of PSD is Cerenkov light generated in the optical fiber that guides the scintillation light.

(iii) Sun nuclear EDGE detector

The sensitive volume of these detectors is made from silicon (Z = 14) which exhibits high sensitivity. The EDGE detector is an n-type shielded diode detector with an active detecting element housed in brass with a 0.13 mm thickness. There is a copper located behind the silicon chip to decrease back scatter reaching the sensitive volume. No bias voltage needs for these detectors when measuring radiation dose. The characteristics of Sun nuclear EDGE are tabulated in Table 5.2.

Table 5.2 Characteristics of W2 PSD and Sun nuclear EDGE

Detector	Material of sensitive volume	Sensitive volume (mm^3)	Diameter of side length of sensitive area (mm)	Thickness of sensitive area (mm)	Geometric form of sensitive area (mm)	Possess shielding material (Yes/No)
Exradin W2 PSD	Polystyrene	0.800	1.0	1.0	Cylinder	No
Sun Nuclear EDGE	Silicon	0.019	0.8	0.03	Square	Yes

5.1.3 Electrometers

To measure the collected charges during the measurement, two electrometers are used in this study: Standard Imaging MAXSD (Standard Imaging, Middleton, USA) and IBA Dose1 electrometer (IBA Dosimetry, Nuremberg, Germany) as shown in Figure 5.3.
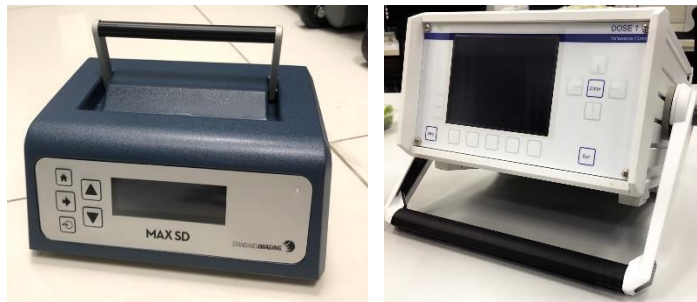
<center>a.</center> <center>b.</center>

Figure 5.3 (a.) MAXSD electrometer (b.) Dose1 electrometer

For Exradin W2 PSD, the photodiode converts the scintillation light transmitted by the optical fiber into an electrical charge. Then the charge is collected by MAX SD electrometer. The MAX SD allows the user to online correct the Čerenkov light that originates within the optic fiber. The electrometer also provides a web interface for point measurement readout. For online Čerenkov correction, the MAX SD separates light from the scintillation detector fiber into two channels. Charge collection mode for channel 1 is mainly for the green light, while Channel 2 collects the signal from blue light. Then, the Čerenkov light correction is done by evaluating the different scintillating light outputs in 10×10 cm^2, with a maximum and minimum length of optic fibers in the field.

The signal from IBA CC01 and Sun nuclear EDGE was measured using the IBA Dose1 electrometer. It is able to measure the electrical charge in the range from 40 pC to 1.0 C at the resolution of 0.1 pC.

5.1.4 Beam scanning system

The three-dimensional (3D) beam scanning water phantom Blue Phantom 2 (IBA Dosimetry, Nuremberg, Germany) is presented in Figure 5.4. A 3D scanning arm can collect beam data along all three axes with positioning accuracy and resolution of ± 0.1 mm. The dimension of the phantom is 48 cm x 48 cm x 41 cm. The scanning arm can be operated via OmniPro-Accept software.

Figure 5.4 IBA Blue Phantom 2

5.1.5 Monte Carlo (MC) simulation software

EGSnrc software is used to determine the field output factor. The BEAMnrc is used to model the linear accelerator treatment head. The DOSXYZnrc is used to create the depth dose and beam profile in a water phantom. The egs_chamber code is applied to calculate the deposited dose in a small voxel of water and the volume of the detector.

5.2 Methods

The methodology of this study involved of small field Monte Carlo (MC) simulation and measurement. The field output correction factor ($k_{Q_{clin},Q_{msr}}^{f_{clin},f_{msr}}$) for elongated small field of IBA CC01 ionization chamber, Sun nuclear EDGE detector, and Exradin w2 PSD was calculated by using EGSnrc MC software. The calculated correction factors were verified with the experiment by measuring the output factor using the same detectors. Then, the output factors were applied to calculated $k_{Q_{clin},Q_{msr}}^{f_{clin},f_{msr}}$ from this study and from TRS 483. For clarity, $k_{Q_{clin},Q_{msr}}^{f_{clin},f_{msr}}$ calculated by MC simulation and TRS 483 were substituted with k_{MC} and k_{TRS}, respectively. The agreement of output factor among three detectors was evaluated in terms of percent standard deviation (%SD).

Although our study focused on the dosimetry of elongated small fields, data on those fields was limited. The majority of published studies have focused on square fields. In order to ensure the accuracy of both measurement and MC simulation, the set of small symmetry field sizes was measured and simulated. Then, the results were compared with the previous studies with the same experiment condition to verify the reliability of our data.

5.2.1 Monte Carlo Simulation

The correction factors; k_{MC} have been calculated with the egs_chamber code. For this purpose, the simulation consisted of four steps. Firstly, the Varian TrueBeam™ treatment head was simulated using BEAMnrc acting as a particle source for egs_chamber. Secondly, the simulated treatment head was evaluated using DOSXYZnrc to compute the dose deposited within the water phantom. Then, the calculated results were compared with measured data through percent depth dose (PDD) and beam profiles as a function of symmetry small field sizes. Thirdly, three detectors were modeled and calculated in egs_chamber. To evaluate the simulated detector, the calculated correction factor; k_{MC} for symmetry small fields were compared with a well-known correction factor from TRS 483; k_{TRS}. Finally, the k_{MC} for elongated small fields were calculated.

(i) Simulation of Varian TrueBeam™ treatment head

The Varian TrueBeam™ version 2 phase-space file of 6 MV photon beam energy was adopted from MyVarian website (https://www.myvarian.com). The phase-space file was generated using GEANT4 MC code with schematics of Varian TrueBeam™ head imported from computer-aided design as an input (38). The phase-space file contains the information of radiation interactions within the linear accelerator treatment head, such as the position, energy, directionality, and type of every particle. The consistency between the phase-space MC results and measured data was reported in several studies (39-41) providing confidence that the phase–space files can be used as a radiation source for accurate MC dose estimation.

Data for the material and geometry of the linear accelerator components below the phase-space plane were taken from the Varian TrueBeam™ Monte Carlo package version 1.1 available on MyVarian website. Figure 5.5 shows the schematics of linear accelerator model simulations by BEAMnrc. The Varian phase-space file was located above the Y jaw at 26.7 cm from the source. Only the X and Y jaws were modeled using JAWS CM. The slab of air was simulated after the X jaw using SLABS CM to create the desired distance between the source and the surface of the phantom. The particles that reach the end of the air slab were stored in the second phase-space file. These field size-specific phase-space files were used as an input source for the subsequent water

phantom simulation in DOSXYZnrc or detectors simulation in egs_chamber. A number of histories ranging from 1×10^9 to 4×10^{10} were used to transport the particles from the location of the Varian phase-space file. In all BEAMnrc simulations, the global ECUT and PCUT were 0.521 MeV and 0.01 MeV, respectively. The particles that total energy less than these values were terminated and deposited their energy in the current voxel. No variance reduction techniques were used. Default settings were applied for all other EGSnrc cross-sectional options and transport parameter values. For details about simulation parameters, see Appendix I.
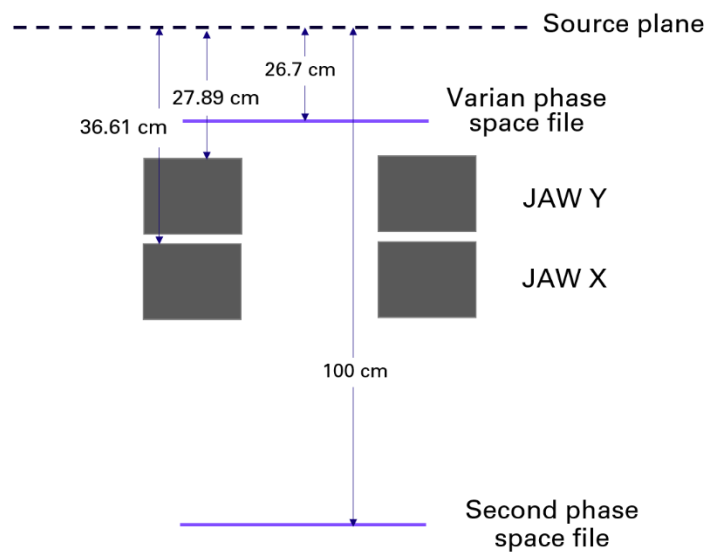
Figure 5.5 Schematic representation of the Varian TrueBeam^{TM} model in BEAMnrc.

(ii) Evaluation of simulated Varian TrueBeam™ head

The Monte Carlo methodology was evaluated by comparing the simulated percentage depth dose (PDD) and beam profile against the measurement. This process used nominal field sizes from 0.6x0.6, 1x1, 2x2, 3x3, 4x4, 6x6, and 10×10 cm^2 for jaw-collimated fields.

To calculate three-dimensional dose distributions in a virtual water phantom, a water phantom size of 30 x 30 x 30 cm^3 was generated using DOSXYZnrc. The voxel sizes were between 0.1 x 0.1 x 0.5 cm^3 and 0.5 x 0.5 x 0.5 cm^3. The resolution of the voxel was varied according to the field size in order to get accurate data of the penumbra. A large enough number of histories were selected for each simulation to keep the statistical uncertainty less than 0.5% at the maximum dose voxel and 0.7% for all the voxels inside the radiation field. The ECUT and PCUT was set to 0.7 and 0.01 MeV, respectively.

The output files that contain the dose deposited in each voxel per number of particles and the associated statistical uncertainty were created as a result of DOSXYZnrc. These files were

exported to MATLAB (The MathWorks, Natick, MA) to calculate the dosimetric quantities. The PDDs and beam profiles were normalized such that a relative comparison between MC simulation and measurements could be done. To calculate the PDD, the dose scoring in voxel along the central beam axis was normalized to the dose at d_{max}. The simulated beam profile was determined by normalizing the dose of voxels at 10 cm depth to the dose on the central axis.

For measurement data, PDDs, cross-plane profiles, and in-plane profiles were acquired in an IBA Blue Phantom 2 with OmniPro‑Accept software. All experiments were set at 100 cm SSD. The PDDs for 6x6 and 10x10 cm^2 fields were measured using IBA CC13. For field sizes smaller than 6x6 cm^2, the Sun Nuclear EDGE detector was used instead. The measured cross-plane and in-plane beam profiles were obtained using the Sun Nuclear EDGE detector scanning across the field area at a depth of 10 cm. Similar to MC simulation, the depth-dose curves were normalized to the depth of maximum dose to calculate the PDD of each field size. At the same time, the beam profiles were normalized to 100% at the central axis to their corresponding field size.

(iii) Simulation and evaluation of detectors

IBA CC01, Sun Nuclear EDGE, and Exradin W2 PSD were modeled using egs_chamber. To evaluate the accuracy of the detector simulation, the correction factors of each detector were calculated for small symmetry fields; 0.6x0.6, 1x1, 2x2, 3x3, 4x4, 6x6, and 10×10 cm^2. Then, the correction factors determined from this study; k_{MC} were compared with the correction factor from TRS 483; k_{TRS}

Three detectors were simulated based on the specifications (technical drawings and information on materials) provided by the manufacturer. The composition and density assignment of detectors were assigned by using data in ICRU Report no. 37 with an electron cutoff energy of AE = 0.521 MeV and a photon energy cutoff AP = 0.01 MeV. To increase the efficiency of the calculation, the variance reduction technique such as photon cross-section enhancement (XCSE) was applied, resulting in the generation of more electrons along the path of the photons tracks within the detector and surrounding material. Default EGSnrc transport parameters were used for all simulations.

The procedure to drive the $k_{Q_{clin},Q_{msr}}^{f_{clin},f_{msr}}$ are recommended by TRS 483 involving experiment and MC simulation. In the latter case, the following equation is used:

$$k_{MC} = \frac{D_{w,Q_{clin}}/D_{w,Q_{msr}}}{D_{det,Q_{clin}}/D_{det,Q_{msr}}} \tag{5.1}$$

Where $D_{w,Q_{clin}}/D_{w,Q_{msr}}$ is the ratio of averaged absorbed dose to small voxel of water for small field and 10x10 cm². The $D_{det,Q_{clin}}/D_{det,Q_{msr}}$ is the ratio of averaged absorbed dose scored in sensitive volume of detector for small field and 10x10 cm².

The sizes of small water voxel were varied according to the field sizes, as shown in Table 5.3. All of the voxel sizes were chosen to avoid the volume averaging effect and prevent the long computation time. The water phantom of 30x30x30 cm³ was created. The small voxel of water or the detectors were put in the water phantom at the central axis of the beam to calculate D_w or D_{det}. All simulations were performed at a depth in water of 10 cm. The number of histories was chosen to achieve a statistical uncertainty of each factor; $D_{w,Q_{clin}}$, $D_{w,Q_{msr}}$, $D_{det,Q_{clin}}$, and $D_{det,Q_{msr}}$ less than 0.3%. Therefore, the total type A statistical uncertainty of the k_{MC} was ~0.5%. Figure 5.6 demonstrates simulated detectors with particle track using egs_chamber.

a.　　　　　　　　　　b.　　　　　　　　　　c.
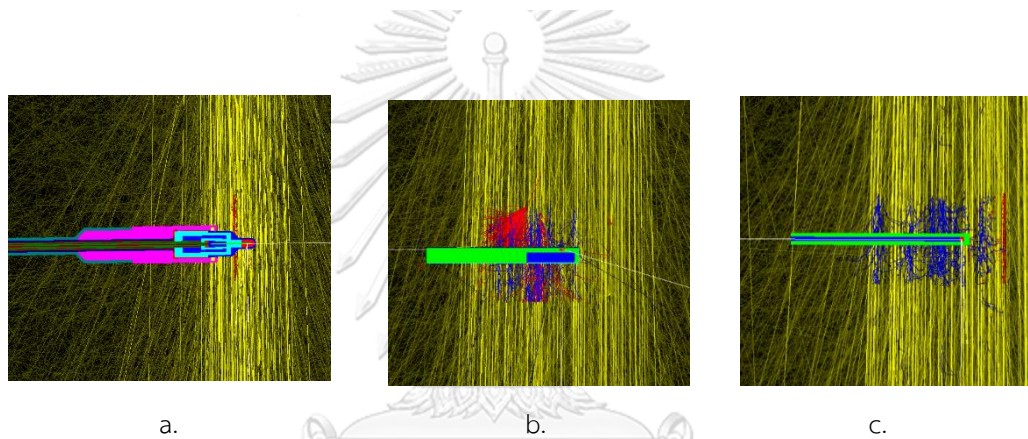
Figure 5.6 Detectors simulated using egs_chamber with particle tracks; (a.) The IBA CC01 (b.) SunNuclear EDGE and (c.) Exradin W2 PSD

Table 5.3 Small voxel of water used for calculating $D_{w,Q_{clin}}$ and $D_{w,Q_{msr}}$ for symmetry small fields

Field sizes (cm²)	Voxel sizes (cm³)
10x10	0.5x0.5x0.2
6x6	
4x4	
3x3	0.15x0.15x0.2
2x2	
1x1	
0.6x0.6	0.1x0.1x0.2

(iv) Determination of k_{MC} for elongated small fields

The correction factor in TRS 483 are tabulated as a function of equivalent square field size (S_{clin}). It is defined as the field that gives the same correction factor as the rectangular or circular small field. The S_{clin} is determined by simply equating the area of field sizes following equation 5.2.

$$S_{clin} = \sqrt{X \times Y}$$ (5.2)

Where X and Y correspond to the in-plane and crosss-plane dosimetric field width defined as the FWHM at the 50% isodose level.

To investigate the S_{clin} proposed in TRS 483, the correction factors were calculated for 2x3, 3x2, 1.5x4, 4x1.5, 1x6, 6x1, 0.6x10, and 10x0.6 cm^2 field sizes. All the field sizes have an equal area of 6 cm^2. Then, the S_{clin} was approximately to 2.4 cm. The degree of the elongation was defined with the ratio of in-plane and cross-plane FWHM (Y/X).

The k_{MC} were calculated using egs_chamber with the same simulation condition used for symmetry small field. Every detector was placed in the in-plane direction (Y axis), the same direction where the measurement was carried out. The size of the small water voxel is presented in Table 5.4.

Table 5.4 Small voxel of water use for calculating $D_{w,Q_{clin}}$ and $D_{w,Q_{msr}}$ for elongated small field.

Field sizes (cm^2)	Voxel sizes (cm^3)
10x10	0.5 x 0.5 x 0.2
2x3	
3x2	0.15 x 0.15 x 0.2
1.5x4	
4x1.5	
1x6	
6x1	0.1 x 0.1 x 0.2
0.6x10	
10x0.6	

5.2.2 Field output factors measurement

(i) Symmetric small field measurement

The measurement of FOF was performed in the IBA Blue water phantom. Dose delivered of 6 MV photon beams generated by Varian TrueBeam™ linear accelerator was measured at 90 cm SSD and 10 cm depth using three detectors: IBA CC01, Sun Nuclear Edge, and Exradin W2 PSD. The calibration of Čerenkov light for Exradin W2 PSD is presented in Appendix II.

The orientation of IBA CC01, Sun Nuclear EDGE, and Exradin W2 PSD were perpendicular to the central beam axis. Each detector was positioned on the central axis of the radiation beam by using in-plane and cross-plane scans to find the position of maximum signal intensity according to TRS 483 guidelines.

Measurements were conducted in seven collimator field sizes: 0.6x0.6, 1x1, 2x2, 3x3, 4x4, 6x6, and 10x10 cm^2. The output reading for a certain field size (M_{clin}) was normalized with the output acquired at 10×10 cm^2 msr field size (M_{msr}).

$$\text{Output reading ratio} = \left[\frac{M_{clin}}{M_{msr}}\right] \qquad (5.3)$$

The FOF was determined by applying the correction factor from Table 26. of TRS 483 with the output reading ratio. The equation 5.1 then becomes

$$\text{FOF} = \left[\frac{M_{clin}}{M_{msr}}\right] \times k_{TRS} \qquad (5.4)$$

The FOF was then compared with previous studies to verify the accuracy of the measurement.

(ii) Elongated small field measurement

The same experiment condition was set to measure the output factor for 2x3, 3x2, 1.5x4, 4x1.5, 1x6, 6x1, 0.6x10, and 10x0.6 cm^2. All of the detectors were placed

in the in-plane direction. Output reading ratio was applied with both k_{MC} and k_{TRS}. In addition, the measured FOF was compared with those calculated by MC simulation in water.

(iii) S_{clin} measurement

The FWHM of symmetric and elongated beam profiles at 10 cm depth was measured using an EDGE detector. The profiles in the X and Y direction were scanned in the water phantom with the highest resolution (0.1 mm) and the lowest scan speed (3 mm/s) to yield the maximum

accuracy in the penumbra region. The dosimetric field width at 50% of the relative dose (FWHM) was recorded. S_{clin} was determined following equation 5.2. For small symmetric field sizes, the S_{clin} of each geometrical field size is assigned through the linear interpolation method to select the k_{TRS}.

CHAPTER 6

RESULTS

6.1 Monte Carlo simulation

(i) Evaluation of simulated Varian TrueBeam™ head

To compare the simulated with measured PDD data, two different evaluation parameters were considered: dose difference in the region beyond d_{max} and distance to agreement (DTA) in the buildup region. The dose difference was prescribed as the percentage dose difference (%DD) between the simulated dose and the measured dose at the same depth. The DTA is the distance between a measurement and the MC calculation point with the same absorbed dose (42). The DTA was calculated with linear interpolation. The percentage depth dose curves of 6 MV photon beam are plotted in Figure 6.1 for 10x10, 6x6, 4x4, 3x3, 2x2, 1x1, and 0.6x0.6 cm^2 fields delivered at 100 cm SSD. The differences between simulation and measurement are included below. In a region deeper than the maximum dose (> 1.5 cm), the measurement and MC simulation data agree closely with a dose difference of less than 2.2%. While the mean dose differences were less than 1.0% for all field sizes. The mean dose difference and standard deviation (SD) between simulated and measured PDDs beyond the buildup region are reported in Table 6.1. In the buildup region, the maximum deviation was found up to 8%. As the buildup region is a high dose gradient region, small spatial shifts between measurement and MC dose distribution can lead to a high dose difference. When DTA was analyzed in the buildup region, we found an agreement of 1.0 mm between MC produced PDD and measurement.

Table 6.1 The mean dose difference and standard deviation of PDDs between simulation and measurement beyond the buildup region. The comparison of PDDs at 10 cm and 20 cm are reported.

Field size (cm^2)	Mean dose difference (%) ± SD	PDD_{10}			PDD_{20}		
		MC	Measured	%Diff	MC	Measured	%Diff
10x10	0.6 ± 0.6	66.4	66.2	0.4	38.0	38.3	-0.9
6x6	0.4 ± 0.5	63.9	63.8	0.2	35.3	35.4	-0.4
4x4	0.4 ± 0.2	62.0	62.1	-0.2	33.5	33.4	0.2
3x3	0.3 ± 0.3	60.3	60.7	-0.7	32.4	32.3	0.4
2x2	0.4 ± 0.2	58.9	59.2	-0.5	31.3	31.5	-0.5
1x1	0.3 ± 0.2	57.2	57.3	0.2	30.3	30.3	-0.3
0.6x0.6	0.7 ± 0.4	55.3	54.8	1.0	29.0	29.0	0.1
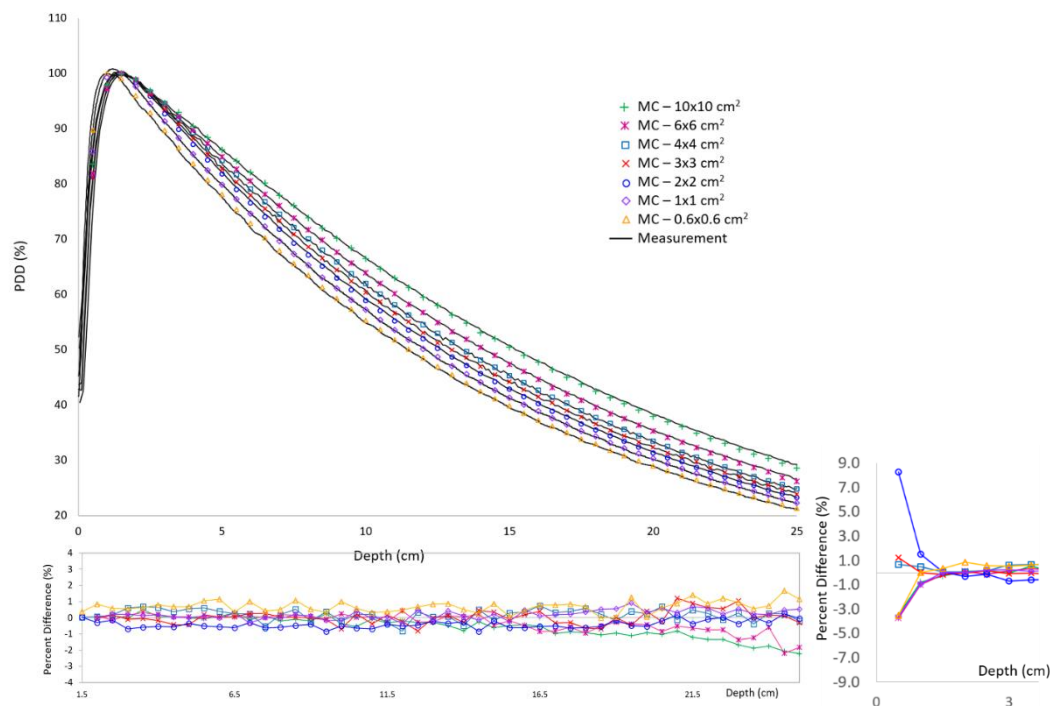
Figure 6.1 Percent depth dose curves for all field sizes. Measurements are plotted as solid lines, while Monte Carlo data are plotted as points. Dose differences beyond d_{max} to 25 cm depth between simulation and measurement are presented in the lower panels. The left lower panel shows dose differenced at d_{max} to 3 cm depth

For the dose profiles, both the cross-plane and in-plane directions were considered. In Figure 6.2, the normalized measured and simulated half-profiles for all field sizes at 10 cm depth are shown. To evaluate the beam profile, the dose difference was analyzed in the radiation field region (within 80% of the normalized dose). The agreement between simulation and measurement in the shoulder and penumbra region (beyond the in-field region) was evaluated by determining the DTA. Table 6.2 demonstrates the dose differences inside the radiation field between measurement and simulation. The mean dose difference was less than or equal to 1.5% for field sizes ≥ 1x1 cm^2. For field sizes ≥ 4x4 cm^2, the deviation was within 1.5% for more than 97% of the points in the radiation field region. For field sizes ≤ 3x3 cm^2, a large deviation was observed. The mean dose differences were found up to 5.0% for 0.6x0.6 cm^2. The discrepancy between simulation and measurement was also found in the profile shoulders. In small field, the profile exhibits a very steep dose gradient, then the flattened region is smaller than 80% of the normalized dose. Therefore, the DTA was applied to evaluate every point of 0.6x0.6, 1x1, and 2x2 cm^2 fields. The DTA of the region where the dose difference exceeded 1.0% was less than 1.0 mm and 1.2 mm for all cross-plane and in-plane profiles, respectively.
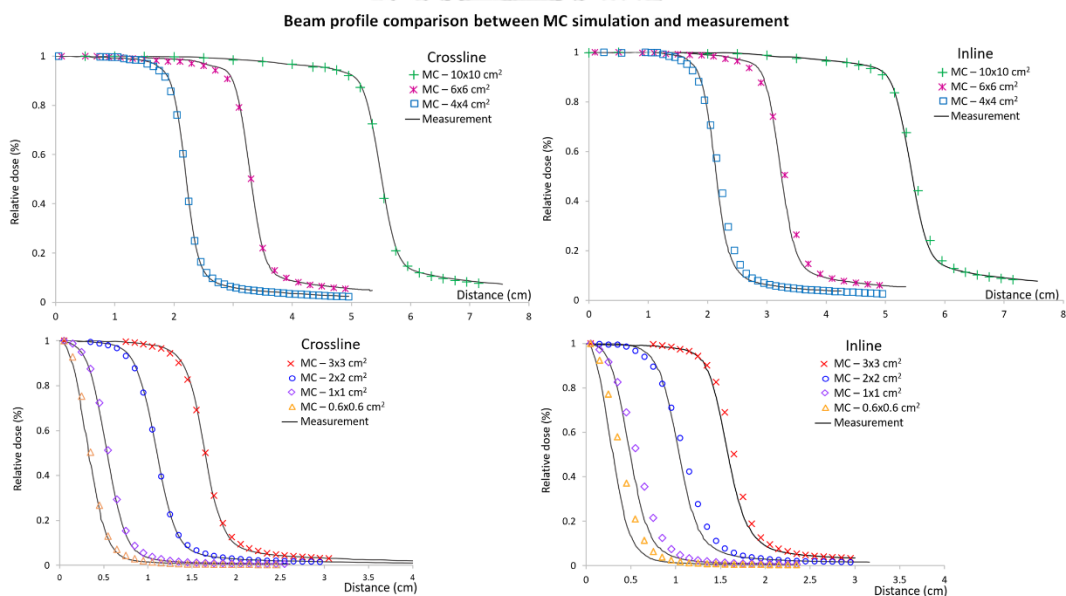
Figure 6.2 Cross-plane (left) and in-plane (right) half profiles for 10x10, 6x6, 4x4, 3x3, 2x2, 1x1, and 0.6x0.6 cm^2. Measurements are plotted as continuous lines, while Monte Carlo data are plotted as point

Table 6.2 Percent difference of the beam profiles between Sun Nuclear Edge measurement and MC simulation inside radiation field. The DTA of the region where the dose difference exceeds ± 1% is shown.

Field sizes (cm^2)	Cross-plane profile		In-plane profile	
	Mean percent dose differences (%) ± SD	DTA (mm)	Mean percent dose differences (%) ± SD	DTA (mm)
10x10	0.2 ± 0.2	0.9	0.3 ± 0.2	0.7
6x6	0.7 ± 0.4	0.8	0.4 ± 0.3	0.9
4x4	0.5 ± 0.4	0.5	0.4 ± 0.4	0.9
3x3	0.5 ± 0.5	0.3	0.3 ± 0.2	0.9
2x2	0.7 ± 0.7	0.6	0.9 ± 0.9	1.2
1x1	0.6 ± 0.7	0.2	1.5 ± 1.4	1.1
0.6x0.6	4.9 ± 3.6	0.7	5.4 ± 3.6	1.2

Other profile characteristics such as FWHM and penumbra were evaluated. The results are summarized in Table 6.3 and 6.4. The FWHM was determined from the distance of 50% relative dose and penumbra was defined as the region between 20% and 80% of the central axis dose. As shown in Table 6.3 and 6.4 the simulated FWHM agrees with measurement within 1.5 mm for field size > 0.6x0.6 cm^2. The deviation of the penumbra was also within 1.5 mm for all field sizes. Overall, the FWHM and penumbra widths tend to be larger than the measurement in the in-plane direction, with the differences increasing with decreasing field size. However, the differences were not exceeded 2.0 mm.

Table 6.3 Comparison of simulated and measured FWHM (distance between 50% isodose level) for different field sizes.

Field sizes (cm^2)	Cross-plane			In-plane		
	FWHM width (mm)			FWHM width (mm)		
	MC	Measurement	Deviation	MC	Measurement	Deviation
10x10	110.0	110.1	0.1	110.0	108.9	1.1
6x6	66.0	66.0	0.0	66.1	64.9	1.2
4x4	44.1	43.9	0.2	44.1	42.9	1.2
3x3	33.0	32.9	0.1	33.1	31.7	1.4
2x2	22.0	22.0	0.0	22.0	20.8	1.2
1x1	11.1	10.8	0.3	11.3	9.9	1.4
0.6x0.6	7.0	6.6	0.4	7.7	6.0	1.7

Table 6.4 Comparison of simulated and measured penumbra width (distance between 20% and 80% isodose level) for different field sizes.

Field sizes (cm^2)	Cross-plane			In-plane		
	Penumbra width (mm)			Penumbra width (mm)		
	MC	Measurement	Deviation	MC	Measurement	Deviation
10x10	5.3	5.5	0.2	6.5	5.6	1.0
6x6	4.6	4.3	0.3	6.0	4.6	1.4
4x4	4.0	3.6	0.4	5.0	3.8	1.2
3x3	3.7	3.4	0.3	4.9	3.8	1.1
2x2	3.6	3.5	0.1	4.6	3.5	1.1
1x1	3.2	3.2	0.0	4.0	3.1	0.9
0.6x0.6	2.8	2.9	0.1	3.3	2.7	0.6

(ii) Evaluation of simulated detectors

To evaluate the simulated detectors, the correction factor calculated from this study; k_{MC} was compared with a well-known correction factor from TRS 483; k_{TRS} through the set of small symmetry field sizes. The results are given in Table 6.5. The k_{MC} was calculate at 10 cm depth with 100 cm SSD. The calculated S_{clin} at 10 cm depth and 100 cm SSD was used for selecting the k_{TRS} from Table 26 of TRS 483. Overall the k_{MC} agree well with the k_{TRS} except CC01 at 0.6x0.6 cm^2 where the difference was ~5%. Only the correction factors of Exradin W1 PSD are given in TRS 483. The Exadin W1 and W2 PSD are similar, but difference in the length of sensitive volume. Galavis *et al.* (43) demonstrated similar dosimetric properties between W1 and W2. Therefore, the correction of 1 for W2 PSD can be assumed.

Table 6.5 Comparison between k_{MC} and k_{TRS} for 6 MV photon energy of IBA CC01, Sun nuclear EDGE, and Exradin W2 PSD. The correction factor for EDGE detector at 0.6x0.6 cm^2 is not provided by TRS 483.

Field size (cm^2)	Calculated S_{clin} (cm)	IBA CC01			Sun nuclear EDGE			Exradin W2 PSD		
		k_{MC}	k_{TRS}	%Diff	k_{MC}	k_{TRS}	%Diff	k_{MC}	k_{TRS}	%Diff
10x10	**11.0**	1.000	1.000	0.0	1.000	1.000	0.0	1.000	1.000	0.0
6x6	**6.61**	1.003	1.003	0.0	1.005	1.000	0.5	0.997	1.000	-0.3
4x4	**4.41**	1.007	1.006	0.0	1.000	1.000	0.0	0.996	1.000	-0.4
3x3	**3.30**	1.007	1.008	0.0	1.000	0.999	0.1	0.999	1.000	-0.1
2x2	**2.20**	1.010	1.009	0.2	0.991	0.996	-0.5	0.996	1.000	-0.4
1x1	**1.12**	1.023	1.015	0.8	0.966	0.972	-0.6	0.999	1.000	-0.1
0.6x0.6	**0.73**	1.084	1.034	4.8	-	N/A	N/A	0.996	1.000	-0.4

(iii) Correction factors of small elongated field

The k_{MC} of IBA CC01, Sun nuclear EDGE, and Exradin W2 PSD for elongated small field are given in Table 6.6. The k_{MC} was calculate at 10 cm depth with 90 cm SSD. The k_{TRS} are also included in the table. As can be seen, k_{TRS} of IBA CC01, Sun nuclear EDGE, and Exradin W2 PSD were nearly the same for all field sizes. The large deviation between k_{MC} and k_{TRS} were found when the field becomes extremely elongated. In this study, the new criterion of the equivalent small field was defined by using the S_{clin} and the minimum side of the field. For example, the elongated field of 0.6x10 cm^2 has the S_{clin}~2.4 cm and the minimum side of the field was 0.6 cm. Then the correction factor for this field was equal to 1.029 for IBA CC01 (Table 6.7).

Table 6.6 MC calculated output correction factors, k_{MC} for IBA CC01, Sun nuclear EDGE, and Exradin W2 PSD at 10 cm depth in water with 90 cm SSD for 6 MV photon beam.

Field size	Calculated	IBA CC01		Sun nuclear EDGE		Exradin W2 PSD	
(cm^2)	S_{clin} (cm)	k_{MC}	k_{TRS}	k_{MC}	k_{TRS}	k_{MC}	k_{TRS}
2 x 3	2.45	1.016	1.008	0.998	0.997	0.999	1.000
3 x 2	2.45	1.003	1.008	0.993	0.997	1.001	1.000
1.5 x 4	2.46	1.013	1.008	0.985	0.998	0.999	1.000
4 x 1.5	2.47	1.014	1.008	0.994	0.997	1.002	1.000
1 x 6	2.48	1.017	1.008	0.973	0.998	1.004	1.000
6 x 1	2.51	1.033	1.008	0.983	0.996	1.006	1.000
0.6 x 10	2.57	1.029	1.008	0.970	0.998	1.011	1.000
10 x 0.6	2.71	1.070	1.008	0.980	0.998	1.008	1.000

Table 6.7 The correction factor of IBA CC01, Sun nuclear EDGE, and Exradin W2 PSD when minimum side of the field was shaped by X or Y jaw for S_{clin}~2.4 cm.

Minimum side of field shaped by X jaw (cm)	S_{clin} (cm)	CC01	EDGE	PSD	Minimum side of field shaped by Y jaw (cm)	S_{clin} (cm)	CC01	EDGE	PSD
0.6	0.66	1.029	0.970	1.011	0.6	0.74	1.070	0.980	1.008
1	1.03	1.017	0.973	1.004	1	1.05	1.033	0.983	1.006
1.5	1.52	1.013	0.987	0.999	1.5	1.52	1.014	0.994	1.002
2	2.00	1.016	0.988	0.999	2	2.01	1.003	0.993	1.001

6.2 Field output factors measurement

(i) Symmetry small field sizes

The FOF determined by using IBA CC01, Sun nuclear EDGE, and Exradin W2 PSD are reported in Table 6.8. The corrections were based on TRS 483 except for 0.6x0.6 cm2 measured with Sun Nuclear EDGE detector, where the correction factor is not provided by TRS 483. Both calculated and measured S_{clin} are included. The difference between measured and MC calculated FOF was less than 1% except for IBA CC01 at 0.6x0.6 cm^2. Figure 6.3 shows measured and calculated FOF and a function of S_{clin}.

Table 6.8 Field output factors measured by using IBA CC01, Sun Nuclear EDGE, and Exradin W2 PSD compared with MC calculated FOF in water.

Field Sizes (cm^2)	S_{clin} (cm)		Field output factors				%Diff compare with water		
	MC calculated	Measured	Water (MC)	CC01	EDGE	PSD	CC01	EDGE	PSD
6x6	5.98	5.98	0.919	0.919	0.919	0.924	0.1	0.1	0.6
4x4	3.99	3.97	0.863	0.862	0.863	0.869	-0.1	-0.1	0.6
3x3	2.99	2.96	0.833	0.829	0.830	0.837	-0.4	-0.3	0.4
2x2	2.00	1.96	0.794	0.788	0.790	0.796	-0.8	-0.5	0.3
1x1	1.04	0.96	0.684	0.678	0.682	0.679	-0.9	-0.3	-0.7
0.6x0.6	0.70	0.61	0.503	0.451	-	0.498	-10.2	-	-0.8
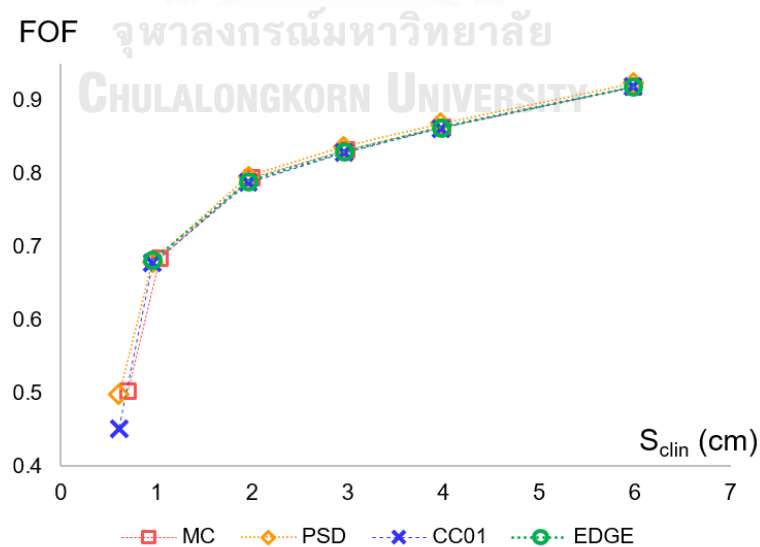
Figure 6.3 The field output factors from MC calculation and measurements plot as a function of S_{clin}.

(ii) Elongated small field sizes

Table 6.9 shows the uncorrected FOF (output ratio) of IBA CC01, Sun nuclear EDGE, and Exradin W2 PSD. The agreement of FOF among three detectors was evaluated in terms of percent standard deviation (%SD) determined following equation 6.1.

$$\% \text{ Standard deviation} = \left[\frac{SD}{Mean}\right] \times 100\% \qquad (6.1)$$

An increase of %SD was discovered by decreasing the side of the field to 1.5 cm, where the maximum %SD was 7.3% at the most elongated field size of 10x0.6 cm^2. The corrected FOF is based on TRS 483; k_{TRS} and correction factor calculated from this work; k_{MC} are given in Table 6.10. For corrected FOF with k_{TRS}, the %SD was slightly decreased for all field sizes. In contrast, the deviation among detectors significantly decreased after implementing the k_{MC} to each detector. In the most elongated field size, the maximum %SD drastically reduced to 3.8%.

Finally, the corrected FOF with both k_{TRS} and k_{MC} were compared with the calculated FOF of water. All data is displayed in Table 6.11. Overall, the difference was comparable for field sizes that were not much elongated (2x3, 3x2, 1.5x4, and 4x1.5 cm^2). When the field was extremely small and long (1x6, 6x1, 0.6x10, 10x0.6 cm^2), the difference of the corrected FOFs with k_{MC} was significantly lower than the corrected FOFs with k_{TRS}.

Table 6.9 Determination of uncorrected field output factors using IBA CC01, Sun nuclear EDGE, and Exradin W2 PSD.

Field sizes (cm^2)	Measured S_{clin} (cm)	Y/X	Uncorrected FOF (output ratio)			
			IBA CC01	Sun nuclear EDGE	W2 PSD	%SD
2 x 3	2.43	1.4	0.802	0.812	0.815	0.7
3 x 2	2.40	0.6	0.798	0.809	0.812	0.7
1.5 x 4	2.45	2.5	0.788	0.805	0.802	0.9
4 x 1.5	2.37	0.3	0.778	0.797	0.795	1.1
1 x 6	2.46	5.8	0.744	0.778	0.763	1.8
6 x 1	2.34	0.2	0.711	0.753	0.740	2.4
0.6 x 10	2.54	15.3	0.631	0.708	0.666	4.7
10 x 0.6	2.40	0.1	0.518	0.617	0.595	7.3

Table 6.10 Determination of field output factors using IBA CC01, Sun nuclear EDGE, and Exradin W2 PSD after correction based on TRS 483 (k_{TRS}) and correction factor calculated from this work (k_{MC}).

Field sizes (cm²)	Y/X	Calculated S_{clin} (cm)	Measured S_{clin} (cm)	FOF corrected with k_{TRS}				FOF corrected with k_{MC}			
				CC01	EDGE	PSD	%SD	CC01	EDGE	PSD	%SD
2 x 3	1.4	2.45	2.43	0.808	0.809	0.815	0.4	0.814	0.811	0.814	0.2
3 x 2	0.6	2.45	2.40	0.804	0.807	0.812	0.4	0.801	0.804	0.812	0.6
1.5 x 4	2.5	2.46	2.45	0.794	0.803	0.802	0.5	0.799	0.793	0.801	0.4
4 x 1.5	0.3	2.47	2.37	0.784	0.794	0.795	0.6	0.789	0.791	0.796	0.4
1 x 6	5.8	2.48	2.46	0.750	0.777	0.763	1.4	0.757	0.757	0.765	0.5
6 x 1	0.2	2.51	2.34	0.717	0.705	0.740	1.9	0.734	0.740	0.744	0.6
0.6 x 10	15.3	2.57	2.54	0.636	0.706	0.666	4.3	0.650	0.686	0.673	2.3
10 x 0.6	0.1	2.71	2.40	0.522	0.616	0.595	6.9	0.554	0.604	0.600	3.8

Table 6.11 Difference between calculated FOF of water and measured FOF corrected with k_{TRS} and k_{MC}.

Field sizes (cm²)	Y/X	MC calculated FOF in water	%Diff of FOF of CC01 when compared with FOF of water		%Diff of FOF of EDGE when compared with FOF of water		%Diff of FOF of PSD when compared with FOF of water	
			corrected with k_{TRS}	corrected with k_{MC}	corrected with k_{TRS}	corrected with k_{MC}	corrected with k_{TRS}	corrected with k_{MC}
2 x 3	1.4	0.821	1.6	0.8	1.1	1.3	0.8	0.8
3 x 2	0.6	0.809	0.6	1.1	0.3	0.7	0.3	0.4
1.5 x 4	2.5	0.806	1.5	1.0	0.4	1.5	0.5	0.6
4 x 1.5	0.3	0.799	1.8	1.2	0.6	0.9	0.5	0.3
1 x 6	5.8	0.768	2.3	1.5	1.1	1.4	0.7	0.3
6 x 1	0.2	0.745	3.8	1.4	0.6	0.7	0.7	0.1
0.6 x 10	15.3	0.671	5.2	3.2	5.2	2.2	0.8	0.3
10 x 0.6	0.1	0.601	13.0	7.7	2.5	0.7	1.0	0.2

CHAPTER 7

DISCUSSION

7.1 Small symmetry field sizes

The focus of this study was to determine the correction factor of IBA CC01, Sun nuclear EDGE, and Exradin W2 PSD for elongated small field sizes. The experiment involved symmetry small field sizes were carried out to ensure the accuracy of dose measurement and simulation for elongated small fields. The symmetry small field sizes were used to evaluate the simulation of Varian TrueBEAM™ treatment head using the Varian phase-space file and the simulation of detectors. The accuracy of the measurement was also validated by measuring the FOF of small symmetry fields.

(i) Evaluation of simulated Varian TrueBeam™ head and simulated detectors

The simulation was done by using Varian phase–space file version 2 of 6 MV photon beam to create the Varian TrueBeam™ treatment head, followed by the simulation of the detectors. The accuracy of the simulated treatment head was evaluated by comparing the resulted PDD, beam profiles, and FOF with measurement. Whereas the simulated detectors were assessed by comparing k_{MC} with k_{TRS}.

Overall, the simulated Varian TrueBeam™ provided consistent data with the measurement. Our result agrees with previous studies that simulated the Varian TrueBeam™ treatment head using the Varian phase-space files. Agreement between all measured and MC simulated PDD data in this study was under 2.2% beyond the buildup region. Bergman *et al.* (39) reported a maximum deviation of 2% between simulated and measured PDD. The mean dose difference ± SD between simulated and measured PDD beyond the buildup region for 10x10, 2x2, 1x1, and 0.6x0.6 cm^2 were comparable with Qin *et al.* (37) as shown in Table 7.1

Table 7.1 Difference of PDD between measurement and MC simulation from this study and Qin et al.(37), who also used a Varian phase-space file with the energy of 6FFF to simulate the TrueBeam^{TM} treatment head.

FS (cm^2)	Mean %dose diff. ± SD	
	This study	Qin *et al.* (37)
10x10	0.6 ± 0.6	0.8 ± 0.5
2x2	0.4 ± 0.2	0.6 ± 0.6
1x1	0.3 ± 0.2	0.6 ± 0.3
0.6x0.6	0.7 ± 0.4	0.1 ± 0.5

The percent difference between simulated and measured PDD was increased up to 2% in the deeper depth, which could be due to the difference in the primary beam energy of the phase-space file and the Varian TrueBeam™ machine in the experiment. However, the error in the deeper depth is not significant in this study since the determination of k_{MC} and field output factor measurement were carried out at 10 cm depth with the percent difference ~1% (Table 6.1.).

For the beam profile, good agreement was observed between measurement and simulation in the in-field dose area for field sizes ≥ 3x3 cm². The DTA of the region where the absolute difference exceeds 1.0% was less than 1.2 mm. Therefore, all simulated data show identical profiles with the measurement within 1.0% of dose difference or 1.2 mm of DTA. The mean dose difference± SD from our study was comparable with Belosi study (Table 7.2).

Table 7.2 Difference of in-field beam profiles between measurement and MC simulation from this study and Belosi et al. (41), who also used Varian phase-space file with the energy of 6FFF to simulate TrueBeam™ treatment head.

FS (cm²)	Mean dose difference (%) ± SD ; In field region		
	This study Cross-plane	This study In-plane	Belosi *et al.* (41)
10x10	0.2 ± 0.2	0.3 ± 0.2	-0.3 ± 0.8
6x6	0.5 ± 0.3	0.4 ± 0.3	-0.2 ± 0.7
3x3	0.5 ± 0.5	0.3 ± 0.2	-0.2 ± 0.7

The maximum difference of the FWHM was 1.7 mm at 0.6x0.6 cm². In comparison, the maximum difference from other studies was ≤ 1.3 mm (39-41, 44). However, the smallest field size that was reported in the published studies was 1x1 cm². A difference of 1.4 mm was found between simulated and measured FWHM in our study at 1x1 cm².

As can be seen, the discrepancy between measurement and simulation in the in-plane was found to be higher than in the cross-plane profile. The widening of the simulated in-plane profile was observed as the field sizes decreased. A possible reason for that discrepancy might be partly ascribed to the difference in the primary photon source width among TrueBeam™ linear accelerators, which were in the range of 1.0 - 1.5 mm (3, 45). According to previous studies, the lateral dose profile of a small field (< 1x1 cm²) was strongly dependent on primary photon source size. Cranmer-Sargison *et al.* (3) reported the dosimetric field widths increase as a function of source size increase. This is due to the partial source occlusion by the collimated jaw and seems to be significantly affected by the upper jaws since it is closer to the source than the lower one.

Excellent agreement between k_{MC} and k_{TRS} was observed for every detector. These ensure the accuracy of the simulated IBA CC01, Sun nuclear Edge, and Exradin W2 PSD detectors. Our values are ~5% larger than the corresponding values from TRS 483 for the IBA CC01 at 0.6x0.6 cm^2 field sizes. It should be noted that obtained k_{TRS} reported in TRS 483 were determined by fitting the entire correction factor from the published studies (experimental and MC) with field size using the analytical function. Other published studies have demonstrated the correction factor of IBA CC01 that exceeded 1.05 when the field size smaller than 1x1 cm^2. Our correction factor of 1.084 was consistent with the work of Yabsantia et $al.$ (46) and Benmakhlouf et $al.$ (19), who reported a correction factor of 1.076 at S_{clin} of 0.6 cm (0.6x0.6 cm^2) and 1.081 at S_{clin} of 0.57 cm(0.5x0.5 cm^2), respectively. In addition, the correction factor of 1.13 was found by Qin et $al.$ (37) The difference in the source size among linac machines which affects the shape of the profile could be the reason for the discrepancy in the correction factor of IBA CC01. For fields smaller than 2x2 cm^2, the output factor drops rapidly with field size. A small change in field size has a dominant effect on the output factor. Another possible reason is the volume averaging effect of the detector. IBA CC01 is consistent with a larger volume averaging effect when compared with other detectors due to its larger sensitive volume (IBA CC01 = 10 mm^3, Sun nuclear EDGE = 0.019 mm^3, and Exradin W2 PSD = 0.08 mm^3). The volume averaging effect leads to the decrease of the detector signal that is averaged over the sensitive volume of the detector. Since the agreement of CC01 was less than 1% for field size >0.6x.6 cm^2, the disagreement between k_{MC} and k_{TRS} at 0.6x0.6 cm^2 could be due to the difference in source size and volume averaging effect rather than an error in detector simulation.

(ii) Measurement of FOF for small symmetry fields

FOF for all small symmetry fields reported in this study and other published studies are given in Table 7.3. These values were measured using TrueBeam^{TM} machine with identical measurement geometry (depth = 10 cm, SSD = 90 cm, JAW defined field sizes). Casar et $al.$ (47) reported that FOF determined by fitting the signal of EBT3 radiochromic films and Exradin W1 PSD by an analytical function. To compare FOF as a function of S_{clin} , FOF from Casar study were interpolate with measured S_{clin} from this work. Mean FOF from Dufreneix et $al.$ (48) was calculated from three TrueBeam^{TM} machines. There is no S_{clin} reported in this literature, the FOF were compared using the nominal field sizes instead. It is found that measured FOF in this study was comparable with the Casar study by 1%. Whereas the agreement was <2% when compared with

Dufreneix *et al.* Figure 7.1 shows FOF measured from this study and Casar *et al.* as a function of S_{clin}.

Table 7.3 Measured field output factors from this study and other studies. All measurements were conducted using Varian TrueBeam^{TM}. FOF from Casar et al. were interpolated by using S_{clin} from this work. For Dufreneix et al., FOF was compared using the nominal field size.

Field sizes (cm^2)	S_{clin} (cm)	Measured FOF (This study)			Casar *et al.* (47)	Dufreneix *et al.* (48)
		EDGE	CC01	PSD	-	-
6x6	5.98	0.919	0.919	0.924	-	-
4x4	3.97	0.863	0.862	0.869	0.864	-
3x3	2.96	0.830	0.829	0.837	0.831	0.836
2x2	1.96	0.790	0.788	0.796	0.789	0.794
1.5x1.5	1.46	0.751	0.757	0.759	0.756	-
1x1	0.96	0.682	0.678	0.679	0.678	0.689
0.6x0.6	0.61	-	0.451	0.498	-	-
0.5x0.5	0.56	-	-	-	0.482	-
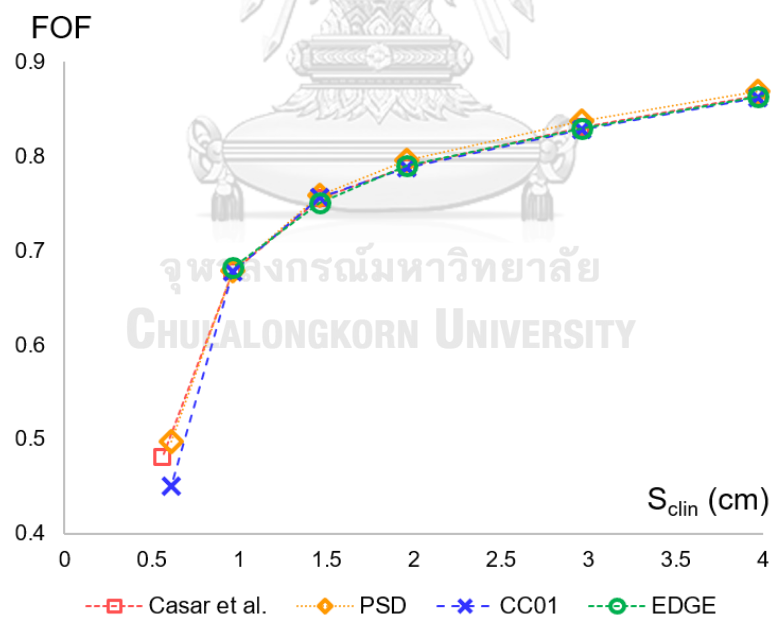
Figure 7.1 Field output factors measured from this study and Casar et al. plot as a function of S_{clin}.

7.2 Elongated small fields

The correction factors of IBA CC01, Sun nuclear EDGE, and Exradin W2 PSD were determined for eight elongated small field sizes using the MC simulation. The elongated fields were shaped by the difference in X and Y jaw, whereas the S_{clin} of all field sizes was ~2.4 cm. The S_{clin} is defined by TRS 483 as the field that either exhibit the same detector perturbation factor or the field output correction factor as the small rectangular field. When the correction factor from our study and TRS 483 were applied, the FOF of three detectors came closer with the reduction of %SD for the field sizes that were nearly symmetry (2x3 and 3x2 cm^2) and moderate elongated (1.5x4, 4x1.5 cm^2). However, when the field sizes were extremely small and elongated (1x6, 6x1, 0.6x10, and 10x0.6 cm^2), %SD of the FOF corrected with k_{TRS} was almost comparable with the uncorrected FOF. When the k_{MC} was applied, the %SD was significantly decreased. Similar results were noticed when compare the corrected FOF with k_{TRS} and k_{MC} with FOF of water calculated using MC simulation. The percent difference was decreased when applied FOF with k_{MC}. TRS 483 recommended to determine the S_{clin} for selecting the correction factor when the field is not too elongated with the ratio of Y/X FWHM in the range between 0.7-1.4. Our results show that the range may be extended up to 0.3-2.5 due to the %SD was less than 1% (Table 6.9) when the FOF was corrected with either k_{TRS} or k_{MC} for 1.5x4 and 4x1.5 cm^2. However, when the field size becomes extremely elongated, the definition of S_{clin} is no longer hold.

The correction factor for the small field has been extensively studied by many authors (19, 20, 22, 23, 46). Most of these studies have focused on symmetry fields. Few studies (23, 37) have reported the correction factor in elongated fields. For the elongated field that composes of small and long side, the side that affects the correction factor should be the smaller one. Figure 7.2 illustrates the overall k_{MC} of three detectors when considering which jaw (X or Y jaw) is defining the minimum aperture opening for a given field.
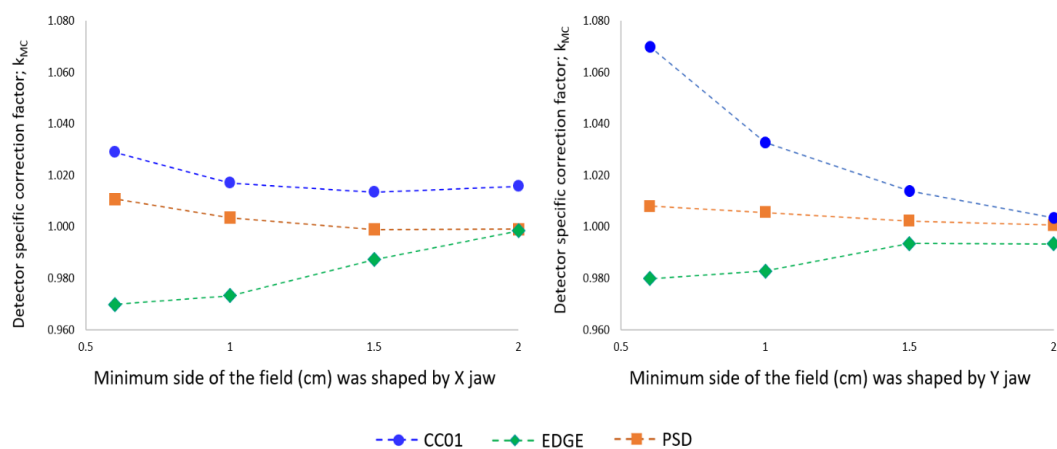
Figure 7.2 Output correction factor of IBA CC01, Sun nuclear EDGE and W2 PSD for 6 MV photon beam as a function of minimum side of the field shaped by X and Y jaw.

IBA CC01 is found to underestimate the beam output for all field sizes as a consequence of the volume averaging effect due to its large air cavity volume compared to field size. The correction factors of IBA CC01 were of the order of 3% and 7% when the smallest side of the field was shaped by X and Y jaw, respectively. Benmakhlouf *et al*. (19) and Yabsantia *et al*. (46) both reported similar under-responses with the IBA CC01 in small symmetry fields.

As can be seen, when the Y jaw was used to shape the smallest side of the field, the correction factors increased rapidly. This could be due to the orientation of the chamber related to its geometry. To determine the correction factor of IBA CC01, the chamber was oriented with its stem perpendicular to the beam and aligned in the Y axis direction. In this case, the cavity length of 3.6 mm was parallel to the Y axis, whereas the shorter cavity diameter of 2 mm was parallel to the X axis. Then, the Y jaw contributed a greater volume averaging effect on the cavity length.

The shielded EDGE diode detector tends to over response due to extra fluence perturbation contributed by the presence of silicon, which has higher stopping power and the brass shielding that increases the fluence of secondary electrons. The corrections factor of Sun nuclear EDGE was less than unity and decreased monotonically with decreasing field size reaching −3% and −2% for X and Y jaws defined the smallest side of the field. The same trend was noticed in the previous studies (23, 35). Either using the X or Y jaw to form the minimum aperture, a similar reduction of the correction factor was observed because the sensitive volume of the detector was symmetry (0.8x0.8 mm) and relatively small. The volume averaging effect is less pronounced in both X and Y direction, but the different penumbra effect in the X and Y profiles affects the correction factor. A higher outcome was observed when the X jaw formed the minimum side of

the field, contributed to the lower correction factor when compared with the Y jaw. Since the lower X jaw is closer to the chamber than the upper Y jaw, it creates the shaper profile (37).

The Exradin W2 PSD has corrections that are close to unity within the total calculation uncertainties at all field sizes. Even for an extremely elongated field, an agreement was within 1%. The measured FOF using the Exradin W2 PSD showed very good agreement <1% with water calculated in the MC simulation. The perturbation correction factors for the PSD were proven to be close to unity by previous studies (20, 36, 49). The detectors exhibit a water equivalent characteristic in terms of atomic composition and electron density. Although those studied were focused on the first-generation plastic scintillator detector (W1 PSD) and only correction factors of Exradin W1 PSD were given in TRS 483. The results reported here are consistent with those for W1 PSD. Exradin W1 and W2 PSD are composed of the same material, but W1 has a longer sensitive volume of 3 mm. A similar dosimetric response for small field dosimetry between W1 and W2 PSD was demonstrated by Galavis *et al.* (43) The main advantage of the W2 PSD over the W1 is its scanning capability in the water phantom. The Exradin W2 PSD have been proven that they are suitable detector not only for small symmetry field but also for an extremely elongated small field.

CHAPTER 8

CONCLUSION

The calculated values of correction factors of IBA CC01, Sun nuclear EDGE, and Exradin PSD W2 are presented for 6 MV photon beams in elongated small fields. The calculated correction factors were verified by the measurements. The comparison between FOF corrected with our correction factor and TRS 483 was made. The %SD reduced significantly when the correction factors from this study were implemented. For IBA CC01 ionization chambers the corrections are up to 7% for the smallest side of the fields. The most important contribution to the correction factor is the volume averaging effect. The correction factor for the EDGE Sun nuclear detector is of the order of -3% for the smallest side of the fields. The correction factors of Exradin W2 PSD are within 1% even for extremely elongated fields due to water equivalence characteristics. The W2 PSD are good candidates for elongated small field commissioning. TRS 483 recommended determining the S_{clin} for selecting the correction factor when the field is not too elongated with the ratio of Y/X FWHM in the range between 0.7-1.4. Our results show that the range may be extended up to 0.3-2.5 due to the %SD was less than 1% when the FOF was corrected with either k_{TRS} or k_{MC} for 1.5x4 and 4x1.5 cm^2. However, when the field size becomes extremely elongated, the definition of S_{clin} is no longer hold. Then, the correction factor should be determined follow TRS 483.

จุฬาลงกรณ์มหาวิทยาลัย

CHULALONGKORN UNIVERSITY

REFERENCES

1.   Das IJ, Ding GX, Ahnesjö A. Small fields: Nonequilibrium radiation dosimetry. Med Phys. 2008;35(1):206-15.

2.   Palmans H, Andreo P, Huq MS, Seuntjens J, Christaki KE, Meghzifene A. Dosimetry of Small Static Fields Used in External Beam Radiotherapy. Vienna: INTERNATIONAL ATOMIC ENERGY AGENCY; 2017.

3.   Cranmer-Sargison G, Charles PH, Trapp JV, Thwaites DI. A methodological approach to reporting corrected small field relative outputs. Radiother Oncol. 2013;109(3):350-5.

4.   Attix FH. Introduction to radiological physics and radiation dosimetry: John Wiley & Sons; 2008.

5.   Nahum A. Perturbation effects in dosimetry: Part I. Kilovoltage x-rays and electrons. Phys Med Biol. 1996;41(9):1531.

6.   Alfonso R, Andreo P, Capote R, Huq MS, Kilby W, Kjäll P, et al. A new formalism for reference dosimetry of small and nonstandard fields. Med Phys. 2008;35(11):5179-86.

7.   Day MJ. A note on the calculation of dose in x-ray fields. Br J Radiol. 1950;23(270):368-9.

8.   McCurdy BM, Pistorius S. Determination of equivalent photon fields through integrated 1D convolution kernels. Phys Med Biol. 1999;44(12):2971-85.

9.   Thomas SJ, Eaton DJ, Tudor GS, Twyman NI. Equivalent squares for small field dosimetry. Br J Radiol. 2008;81(971):897-901.

10.   Clarkson J. A Note on Depth Doses in Fields of Irregular Shape. Br J Radiol. 1941;14:265-8.

11.   Meredith WJ, Neary G. The production of isodose curves and the calculation of energy absorption from standard depth dose data. Br J Radiol. 1944;17(195):75-82.

12.   Sterling TD, Perry H, Katz L. Automation of radiation treatment planning—IV. Derivation of a mathematical expression for the per cent depth dose surface of cobalt 60 beams and visualisation of multiple field dose distributions. Br J Radiol. 1964;37(439):544-50.

13.   Sathiyan S, Ravikumar M, Keshava S. Relative output factors and absolute equivalent square fields at depths for high energy x-ray and gamma ray beams. Austral Asian Journal of Cancer. 2006;5(4):225-35.

14.   McKerracher C, Thwaites DI. Phantom scatter factors for small MV photon fields. Radiother Oncol. 2008;86(2):272-5.

15.   Cranmer-Sargison G, Weston S, Sidhu NP, Thwaites DI. Experimental small field 6MV output ratio analysis for various diode detector and accelerator combinations. Radiother Oncol. 2011;100(3):429-35.

16.   Seco J, Verhaegen F. Monte Carlo Techniques in Radiation Therapy: Taylor & Francis Group; 2016.

17.   Chetty I. Monte Carlo Treatment Planning—An Introduction: Report 16 of the Netherlands Commission on Radiation Dosimetry. Med Phys. 2008;35(11):5198-9.

18. Chetty IJ, Curran B, Cygler JE, DeMarco JJ, Ezzell G, Faddegon BA, et al. Report of the AAPM Task Group No. 105: Issues associated with clinical implementation of Monte Carlo-based photon and electron external beam treatment planning. Med Phys. 2007;34(12):4818-53.

19. Benmakhlouf H, Sempau J, Andreo P. Output correction factors for nine small field detectors in 6 MV radiation therapy photon beams: a PENELOPE Monte Carlo study. Med Phys. 2014;41(4):041711.

20. Francescon P, Kilby W, Satariano N. Monte Carlo simulated correction factors for output factor measurement with the CyberKnife system—results for new detectors and correction factor dependence on measurement distance and detector orientation. Phys Med Biol. 2014;59(6):N11-N7.

21. Cranmer-Sargison G, Weston S Fau - Evans JA, Evans Ja Fau - Sidhu NP, Sidhu Np Fau - Thwaites DI, Thwaites DI. Implementing a newly proposed Monte Carlo based small field dosimetry formalism for a comprehensive set of diode detectors. (0094-2405 (Print)).

22. Girardi A, Fiandra C, Giglioli FR, Gallio E, Ali OH, Ragona R. Small field correction factors determination for several active detectors using a Monte Carlo method in the Elekta Axesse linac equipped with circular cones. Phys Med Biol. 2019;64(11):11nt01.

23. Francescon P, Cora S, Satariano N. Calculation of k(Q(clin),Q(msr)) (f(clin),f(msr)) for several small detectors and for two linear accelerators using Monte Carlo simulations. Med Phys. 2011;38(12):6513-27.

24. Verhaegen F, Seuntjens J. Monte Carlo modelling of external radiotherapy photon beams. Phys Med Biol. 2003;48(21):R107-64.

25. Kawrakow I. The EGSnrc Code System, Monte Carlo Simulation of Electron and photon Transport. NRCC Report PIRS-701. 2001.

26. Rogers D, Kawrakow I, Seuntjens J, Walters B, Mainegra-Hing E. NRC user codes for EGSnrc. NRCC Report PIRS-702 (Rev B). 2003.

27. Rogers D, Walters B, Kawrakow I. BEAMnrc users manual. Nrc Report Pirs. 2009;509:12.

28. Walters B, Kawrakow I, Rogers D. DOSXYZnrc users manual. Nrc Report Pirs. 2005;794:57-8.

29. Knoll GF. Radiation Detection and Measurement: Wiley; 2010.

30. Andreo P, Burns DT, Nahum AE, Seuntjens J, Attix FH. Fundamentals of Ionizing Radiation Dosimetry: Wiley; 2017.

31. Beddar S, Beaulieu L. Scintillation Dosimetry: CRC Press; 2016.

32. Liu PZ, Suchowerska N, Lambert J, Abolfathi P, McKenzie DR. Plastic scintillation dosimetry: comparison of three solutions for the Cerenkov challenge. Phys Med Biol. 2011;56(18):5805-21.

33. Wang LL, Beddar S. Study of the response of plastic scintillation detectors in small-field 6 MV photon beams by Monte Carlo simulations. Med Phys. 2011;38(3):1596-9.

34. Lechner W, Palmans H, Sölkner L, Grochowska P, Georg D. Detector comparison for small field output factor measurements in flattening filter free photon beams. Radiother Oncol. 2013;109(3):356-60.

35. Tanny S, Sperling N, Parsai EI. Correction factor measurements for multiple detectors used in small field dosimetry on the Varian Edge radiosurgery system. (2473-4209 (Electronic)).

36.   Morin J, Béliveau-Nadeau D, Chung E, Seuntjens J, Thériault D, Archambault L, et al. A comparative study of small field total scatter factors and dose profiles using plastic scintillation detectors and other stereotactic dosimeters: The case of the CyberKnife. Med Phys. 2013;40(1):011719.

37.   Qin Y, Zhong H, Wen N, Snyder K, Huang Y, Chetty IJ. Deriving detector-specific correction factors for rectangular small fields using a scintillator detector. J Appl Clin Med Phys. 2016;17(6):379-91.

38.   Constantin M, Perl J, LoSasso T, Salop A, Whittum D, Narula A, et al. Modeling the truebeam linac using a CAD to Geant4 geometry implementation: dose and IAEA-compliant phase space calculations. Med Phys. 2011;38(7):4018-24.

39.   Bergman AM, Gete E, Duzenli C, Teke T. Monte Carlo modeling of HD120 multileaf collimator on Varian TrueBeam linear accelerator for verification of 6X and 6X FFF VMAT SABR treatment plans. J Appl Clin Med Phys. 2014;15(3):4686.

40.   Gete E, Duzenli C, Milette M-P, Mestrovic A, Hyde D, Bergman AM, et al. A Monte Carlo approach to validation of FFF VMAT treatment plans for the TrueBeam linac. Med Phys. 2013;40(2):021707.

41.   Belosi MF, Rodriguez M, Fogliata A, Cozzi L, Sempau J, Clivio A, et al. Monte Carlo simulation of TrueBeam flattening-filter-free beams using Varian phase-space files: Comparison with experimental data. Med Phys. 2014;41(5):051707.

42.   Low DA, Dempsey JF. Evaluation of the gamma dose distribution comparison method. Med Phys. 2003;30(9):2455-64.

43.   Galavis PE, Hu L, Holmes S, Das IJ. Characterization of the plastic scintillation detector Exradin W2 for small field dosimetry. Med Phys. 2019;46(5):2468-76.

44.   Teke T, Duzenli C, Bergman A, Viel F, Atwal P, Gete E. Monte Carlo validation of the TrueBeam 10XFFF phase–space files for applications in lung SABR. Med Phys. 2015;42(12):6863-74.

45.   Papaconstadopoulos P, Levesque IR, Aldelaijan S, O'Grady K, Devic S, Seuntjens J. Modeling the primary source intensity distribution: reconstruction and inter-comparison of six Varian TrueBeam sources. Phys Med Biol. 2019;64(13):135005.

46.   Yabsantia S, Suriyapee S, Phaisangittisakul N, Oonsiri S, Sanghangthum T, Mirzakhanian L, et al. Determination of field output correction factors of radiophotoluminescence glass dosimeter and CC01 ionization chamber and validation against IAEA-AAPM TRS-483 code of practice. Phys Med. 2021;88:167-74.

47.   Casar B, Gershkevitsh E, Mendez I, Jurković S, Huq MS. A novel method for the determination of field output factors and output correction factors for small static fields for six diodes and a microdiamond detector in megavoltage photon beams. Med Phys. 2019;46(2):944-63.

48.   Dufreneix S, Bellec J, Josset S, Vieillevigne L. Field output factors for small fields: A large multicentre study. Phys Med. 2021;81:191-6.

49.   Papaconstadopoulos P, Tessier F, Seuntjens J. On the correction, perturbation and modification of small field detectors in relative dosimetry. Phys Med Biol. 2014;59(19):5937.

50.   Carrasco P, Jornet N, Jordi O, Lizondo M, Latorre-Musoll A, Eudaldo T, et al. Characterization of the Exradin W1 scintillator for use in radiotherapy. Med Phys. 2015;42(1):297-304.

51.   Guillot M, Gingras L, Archambault L, Beddar S, Beaulieu L. Spectral method for the correction of the Cerenkov light effect in plastic scintillation detectors: a comparison study of calibration procedures and validation in Cerenkov light-dominated situations. Med Phys. 2011;38(4):2140-50.

APPENDIX I

EGSnrc transport parameter

Global ECUT= 0.521

Global PCUT= 0.01

Global SMAX= 1e01

ESTEPE= 0.25

XIMAX= 0.5

Boundary crossing algorithm= EXACT

Skin depth for BCA= 0

Electron-step algorithm= PRESTA-II

Spin effects= On

Brems angular sampling= Simple

Brems cross sections= BH

Bound Compton scattering= Off

Compton cross sections= default

Pair angular sampling= Simple

Pair cross sections= BH

Photoelectron angular sampling= Off

Rayleigh scattering= Off

Atomic relaxations= Off

Electron impact ionization= Off

Photon cross sections= xcom

Photon cross-sections output= Off

APPENDIX II

Determination of Čerenkov light ratio

Čerenkov light is produced in optical fibers when charged particles enter the core with speed greater than the speed of light. The amount of Čerenkov light also depends on the length of the irradiated fiber. To subtract the Čerenkov light, one of the most widely techniques (50) is to use the spectral difference between the light generated in the scintillator and the Čerenkov light. This refers to blue and green light that emits from the irradiated scintillating and optic fiber. It is seen in Figure II.1 that the wavelength of Čerenkov light is very broad, which covers the blue and green spectrum. In contrast, the scintillating fiber produces light mainly in the blue wavelength.
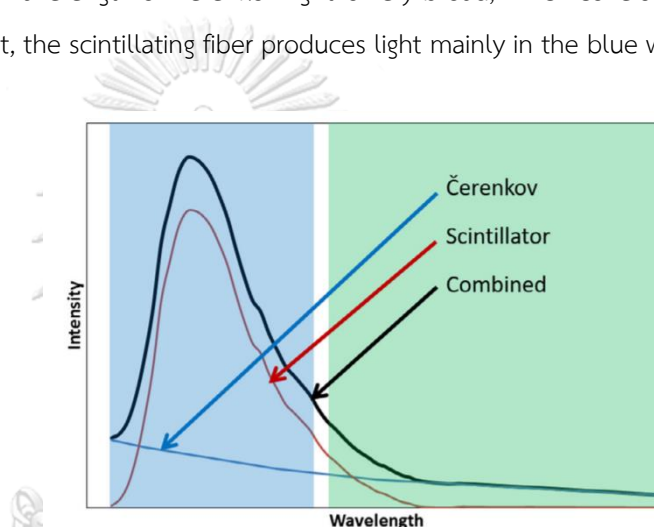
Figure II.3 Schematic of the scintillator and Čerenkov radiation spectra along with the blue and green filter regions.

We followed the calibration procedure recommended by the manufacturer. The procedure consists of the determination of the Čerenkov Light Ratio (CLR) and the Gain value (calibration factor). The CLR is the process that removes the Čerenkov Light from the scintillating light based on the method proposed by Gulliot *et al.* (51) This method requires two measurements in which the dose to the scintillator remains constant, but the length of optical fiber in the field changes. Then, the difference in measured signal between two configurations depends on only the magnitude of Čerenkov emissions.

In this process, a Varian TrueBeam^{TM} linac provided the photon beam of 6 MV was used. The output of the accelerator was calibrated so that 1 MU delivered 1 cGy at a depth of maximum dose (d_{max}) with a 10×10 cm^2 field at 100 SSD. The optic fiber of the W2 PSD was arranged to maximum and minimum fiber configuration using a calibration bracket (Figure II.2). Both fiber

configuration was irradiated with a fixed number of monitor units under the same field size of 10x10 cm^2 at d$_{max}$. The solid water phantom with a thickness of 20 cm was used to create the depth beyond the W2 PSD. The detector was placed between a 1.5 cm thick bolus. According to the manufacturer's specifications, the CLR was calculated following equation II.1

$$CLR = \frac{Blue_{max} - Blue_{min}}{Green_{max} - Green_{min}}$$

(II.1)

Where max and min refer to the signals for a maximum and minimum length of optic fiber that was irradiated. $Blue$ and $Green$ were the light that emitted when radiation interacted with scintillating fiber (Figure II.2).

Maximum fiber   Minimum fiber
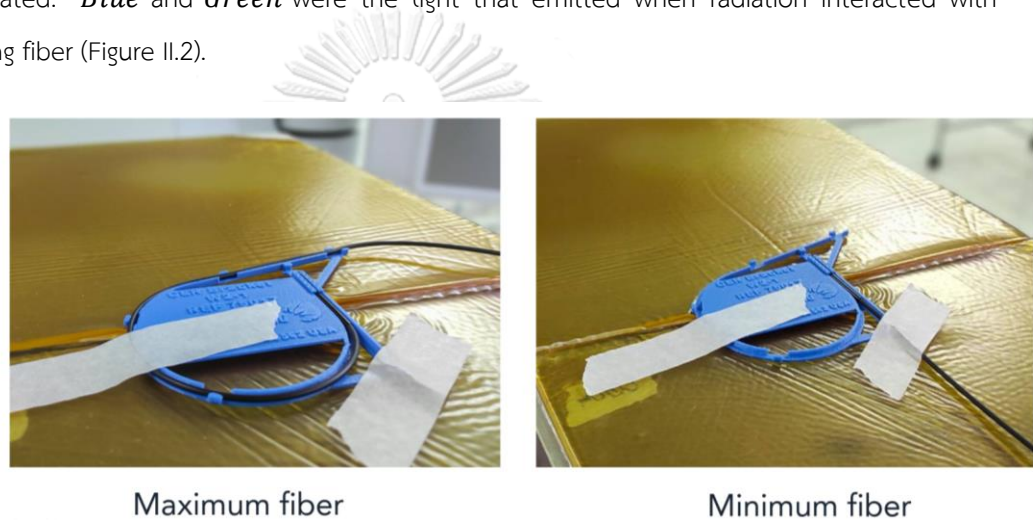
Figure II.4 Calibration bracket with the W2 PSD in the maximum fiber configuration (left) and minimum fiber configuration (right).

To determine the $Gain$ value, the minimum fiber configuration was set using a calibration bracket. The detector was placed at d$_{max}$ in the solid water phantom. When the detector was exposed to a known radiation dose (D_{ref}), the $Gain$ can be calculated following equationII.2.

$$Gain = D_{ref} \times (Blue_{ref} - CLR \times Green_{ref})$$

(II.2)

Once these parameters are determined, the dose for any situation can be calculated from the charge converted from the blue and the green light.

$$D = Gain \times (Blue - CLR \times Green)$$

(II.3)

APPENDIX III

Data of Monte Carlo simulation

The raw data of dose per particle calculated in water and sensitive volume of the detectors for symmetry and elongated small fields are presented in Table III.1-III.8.

Table III.1 Dose per particles in small voxel volumes for symmetry small field at a depth of 10 cm and 100 cm SSD.

Field size (cm^2)	S_{clin} (cm)	Dose/particle (cGy/particle)	Uncertainty (%)	Ratio
10x10	11.0	9.568 E-17	0.25	1.000
6x6	6.6	8.788 E-17	0.20	0.919
4x4	4.4	8.261 E-17	0.22	0.863
3x3	3.3	8.006 E-17	0.24	0.837
2x2	2.2	7.599 E-17	0.17	0.794
1x1	1.1	6.544 E-17	0.33	0.684
0.6x0.6	7.3	4.808 E-17	0.28	0.503

Table III.2 Dose per particles in sensitive volume of Sun Nuclear EDGE detector for symmetry small field at a depth of 10 cm and 100 cm SSD.

Field size (cm^2)	S_{clin} (cm)	Dose/particle (cGy/particle)	Uncertainty (%)	Ratio
10x10	11.0	9.719 E-17	0.35	1.000
6x6	6.6	8.886 E-17	0.29	0.914
4x4	4.4	8.388 E-17	0.28	0.863
3x3	3.3	8.098 E-17	0.25	0.833
2x2	2.2	7.793 E-17	0.26	0.802
1x1	1.1	6.881 E-17	0.26	0.708

Table III.3 Dose per particles in sensitive volume of Exradin W2 PSD for symmetry small field at a depth of 10 cm and 100 cm SSD.

Field size (cm^2)	S_{clin} (cm)	Dose/particle (cGy/particle)	Uncertainty (%)	Ratio
10x10	11.0	9.183 E-17	0.28	1.000
6x6	6.6	8.464 E-17	0.24	0.922
4x4	4.4	7.957 E-17	0.24	0.867
3x3	3.3	7.658 E-17	0.24	0.834
2x2	2.2	7.321 E-17	0.27	0.797
1x1	1.1	6.287 E-17	0.26	0.685
0.6x0.6	7.3	4.633 E-17	0.28	0.505

Table III.4 Dose per particles in sensitive volume of IBA CC01 for symmetry small field at a depth of 10 cm and 100 cm SSD.

Field size (cm^2)	S_{clin} (cm)	Dose/particle (cGy/particle)	Uncertainty (%)	Ratio
10x10	11.0	8.877 E-17	0.30	1.000
6x6	6.6	8.128 E-17	0.40	0.916
4x4	4.4	7.615 E-17	0.32	0.858
3x3	3.3	7.342 E-17	0.28	0.827
2x2	2.2	6.977 E-17	0.22	0.786
1x1	1.1	5.934 E-17	0.22	0.669
0.6x0.6	7.3	4.115 E-17	0.27	0.464

Table III.5 Dose per particles in small voxel volumes for elongated small field at a depth of 10 cm and 90 cm SSD.

Field size (cm^2)	S_{clin} (cm)	Dose/particle (cGy/particle)	Uncertainty (%)	Ratio
10x10	10.0	1.139E-16	0.23	1.000
2x3	2.5	9.351E-17	0.22	0.821
3x2	2.4	9.220E-17	0.22	0.809
1.5x4	2.5	9.185E-17	0.20	0.806
4x.15	2.5	9.098E-17	0.20	0.799
1x6	2.5	8.747E-17	0.23	0.768
6x1	2.5	8.485E-17	0.21	0.745
0.6x10	2.6	7.646E-17	0.23	0.671
10x0.6	2.7	6.840E-17	0.22	0.601

Table III.6 Dose per particles in sensitive volume of Sun Nuclear EDGE detector for elongated small field at a depth of 10 cm and 90 cm SSD.

Field size (cm²)	S_{clin} (cm)	Dose/particle (cGy/particle)	Uncertainty (%)	Ratio
10x10	10.0	1.154 E-16	0.22	1.000
2x3	2.5	9.487 E-17	0.24	0.822
3x2	2.4	9.402 E-17	0.25	0.815
1.5x4	2.5	9.424 E-17	0.20	0.817
4x.15	2.5	9.276 E-17	0.22	0.804
1x6	2.5	9.104 E-17	0.25	0.789
6x1	2.5	8.746 E-17	0.24	0.758
0.6x10	2.6	7.985 E-17	0.23	0.692
10x0.6	2.7	7.071 E-17	0.23	0.613

Table III.7 Dose per particles in sensitive volume of Exradin W2 PSD for elongated small field at a depth of 10 cm and 90 cm SSD.

Field size (cm²)	S_{clin} (cm)	Dose/particle (cGy/particle)	Uncertainty (%)	Ratio
10x10	10.0	1.097E-16	0.22	1.000
2x3	2.5	9.013E-17	0.23	0.822
3x2	2.4	8.873E-17	0.25	0.809
1.5x4	2.5	8.854E-17	0.28	0.807
4x.15	2.5	8.741E-17	0.23	0.797
1x6	2.5	8.394E-17	0.23	0.765
6x1	2.5	8.125E-17	0.23	0.741
0.6x10	2.6	7.284E-17	0.24	0.664
10x0.6	2.7	6.534E-17	0.24	0.596

Table III.8 Dose per particles in sensitive volume of IBA CC01 for elongated small field at a depth of 10 cm and 90 cm SSD.

Field size (cm^2)	S$_{clin}$ (cm)	Dose/particle (cGy/particle)	Uncertainty (%)	Ratio
10x10	10.0	1.058E-16	0.23	1.000
2x3	2.5	8.554E-17	0.23	0.808
3x2	2.4	8.537E-17	0.24	0.807
1.5x4	2.5	8.420E-17	0.23	0.796
4x.15	2.5	8.337E-17	0.22	0.788
1x6	2.5	7.991E-17	0.27	0.755
6x1	2.5	7.634E-17	0.22	0.721
0.6x10	2.6	6.904E-17	0.23	0.652
10x0.6	2.7	5.940E-17	0.23	0.561

APPENDIX IV

Data from field output factor measurement

The raw data from field output factor measurement using IBA CC01, Sun Nuclear EDGE, and Exradin W2 PSD for symmetry and elongated small fields are presented in Table IV.1-IV.6.

Table IV.1 Meter reading measured by IBA CC01 for symmetry small field at a depth of 10 cm and 90 cm SSD.

Field size (cm^2)	S_{clin} (cm)	1 (nC)	2 (nC)	3 (nC)	Avg	Ratio
10x10	10.00	0.727	0.728	0.727	0.727	1.000
6x6	5.98	0.665	0.666	0.666	0.666	0.915
4x4	3.97	0.623	0.623	0.623	0.623	0.856
3x3	2.96	0.598	0.598	0.599	0.598	0.823
2x2	1.96	0.568	0.568	0.567	0.568	0.781
1.5x1.5	1.46	0.539	0.540	0.540	0.540	0.742
1x1	0.96	0.483	0.484	0.484	0.483	0.665
0.6x0.6	0.61	0.314	0.314	0.314	0.314	0.431

Table IV.2 Meter reading measured by Sun nuclear EDGE for symmetry small field at a depth of 10 cm and 90 cm SSD.

Field size (cm^2)	S_{clin} (cm)	1 (nC)	2 (nC)	3 (nC)	Avg	Ratio
10x10	10.00	32.45	32.46	32.46	32.46	1.000
6x6	5.98	29.84	29.83	29.83	29.83	0.919
4x4	3.97	27.99	28.00	28.01	28.00	0.863
3x3	2.96	26.97	26.98	26.97	26.97	0.831
2x2	1.96	25.82	25.83	25.83	25.83	0.796
1.5x1.5	1.46	24.96	24.95	24.93	24.95	0.769
1x1	0.96	22.99	22.99	22.99	22.99	0.708
0.6x0.6	0.61	17.69	17.71	17.70	17.70	0.545

Table IV.3 Meter reading measured by Exradin W2 PSD for symmetry small field at a depth of 10 cm and 90 cm SSD.

Field size (cm²)	S_{clin} (cm)	1 (nC)	2 (nC)	3 (nC)	Avg	Ratio
10x10	10.00	76.76	76.83	76.88	76.82	1.000
6x6	5.98	71.02	70.95	71.04	71.003	0.924
4x4	3.97	66.74	66.77	66.73	66.745	0.869
3x3	2.96	64.30	64.23	64.30	64.278	0.837
2x2	1.96	61.20	61.11	61.22	61.180	0.796
1.5x1.5	1.46	58.21	58.26	58.38	58.283	0.759
1x1	0.96	52.27	52.20	52.13	52.199	0.679
0.6x0.6	0.61	38.26	38.33	38.300	38.295	0.498

Table IV.4 Meter reading measured by IBA CC01 for elongated small field at a depth of 10 cm and 90 cm SSD.

Field size (cm²)	S_{clin} (cm)	1 (nC)	2 (nC)	3 (nC)	Avg	Ratio
0.6x10	2.54	0.459	0.460	0.459	0.459	0.631
1x6	2.46	0.541	0.542	0.541	0.541	0.744
1.5x4	2.45	0.573	0.574	0.572	0.573	0.788
2x3	2.43	0.583	0.583	0.583	0.583	0.802
3x2	2.40	0.580	0.581	0.580	0.580	0.798
4x1.5	2.37	0.566	0.566	0.566	0.566	0.778
6x1	2.34	0.517	0.516	0.518	0.517	0.711
10x0.6	2.40	0.377	0.377	0.377	0.377	0.518

Table IV.5 Meter reading measured by Sun Nuclear EDGE for elongated small field at a depth of 10 cm and 90 cm SSD.

Field size (cm²)	S$_{clin}$ (cm)	1 (nC)	2 (nC)	3 (nC)	Avg	Ratio
0.6x10	2.54	22.96	22.96	22.98	22.97	0.708
1x6	2.46	25.26	25.27	25.24	25.26	0.778
1.5x4	2.45	26.10	26.12	26.15	26.12	0.805
2x3	2.43	26.36	26.35	26.35	26.35	0.812
3x2	2.40	26.28	26.26	26.28	26.27	0.809
4x1.5	2.37	25.87	25.82	25.87	25.86	0.797
6x1	2.34	24.43	24.44	24.43	24.43	0.753
10x0.6	2.40	20.01	20.03	20.03	20.02	0.617

Table IV.6 Meter reading measured by Exradin W2 PSD for elongated small field at a depth of 10 cm and 90 cm SSD.

Field size (cm²)	S$_{clin}$ (cm)	1 (nC)	2 (nC)	3 (nC)	Avg	Ratio
0.6x10	2.54	51.07	51.25	51.15	51.16	0.666
1x6	2.46	58.59	58.60	58.57	58.59	0.763
1.5x4	2.45	61.61	61.64	61.66	61.64	0.802
2x3	2.43	62.57	62.58	62.64	62.60	0.815
3x2	2.40	62.40	62.33	62.41	62.38	0.812
4x1.5	2.37	61.01	61.06	61.07	61.04	0.795
6x1	2.34	56.89	56.82	56.846	56.85	0.740
10x0.6	2.40	45.69	45.69	45.69	45.69	0.595

APPENDIX IV

IRB Certification

COE No. 010/2022

IRB No. 0108/65

INSTITUTIONAL REVIEW BOARD

Faculty of Medicine, Chulalongkorn University

1873 Rama IV Road, Patumwan, Bangkok 10330, Thailand, Tel 662-256-4493
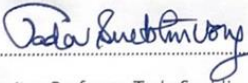
Certificate of Exemption

(COE No. 010/2022)

The Institutional Review Board of the Faculty of Medicine, Chulalongkorn University, Bangkok, Thailand, has exempted the following study in compliance with the International guidelines for human research protection as Declaration of Helsinki, The Belmont Report, CIOMS Guideline, International Conference on Harmonization in Good Clinical Practice (ICH-GCP) and 45CFR 46.101(b)

Study Title : Determination of field output correction factors in elongated small field photon beams

Principal Investigator : Miss Mananchaya Vimolnoch

Study Center : Department of Radiology, Faculty of Medicine, Chulalongkorn University.

Signature : .... Signature : ....

(Emeritus Professor Tada Sueblinvong MD) (Assistant Professor Thananya Thongtan PhD)

Chairperson Member and Secretary

The Institutional Review Board The Institutional Review Board

Date of Exemption : February 14, 2022

<u>Note</u> 1. Continuing review report is not required.

2. Any changes or modifications of the exempted research proposal, required the submission of amendments to Med Chula IRB.

3. Final report is required after completion.

VITA

NAME	Mananchaya Vimolnoch
DATE OF BIRTH	23 December 1992
PLACE OF BIRTH	Bangkok, Thailand
INSTITUTIONS ATTENDED	2011 – 2015 Bachelor of Science (Radiological Technology) Faculty of Medical Technology, Mahidol University GPA 3.43

2016-2018   Master of Science (Medical Imaging) Faculty of Medicine, Chulalongkorn University

GPA 3.98

Thesis: Measurement of eye lens dose in interventional radiologist from TACE procedure using OSLD.

2018-Present   Resident in IAEA Project RAS 6087: Enhancing Medical Physics Services in Developing Standards, Education and Training through Regional Cooperation (RCA) in radiation oncology medical physics

Ph.D. student in Medical Physics program, Faculty of Medicine, Chulalongkorn University

HOME ADDRESS	39 Sukhumvit 81,Phrakanongnue, Wattana, Bangkok, Thailand 10260
PUBLICATION	1. Vimolnoch M., Krisanachinda A. Estimated eye lens dose of interventional radiologist using OSLD: Phantom study in Proceeding of 15th South East Asia Congress of Medical Physics, pp., Philippines, 2017

2. Vimolnoch M., Krisanachinda A. Measurement of eye lens doses of interventional radiologists using OSLDs in Proceeding of 10th Annual Scientific of Thai Medical Physicist Society (TMPS), Bangkok, Thailand 2018

3. Oonsiri P., Vannavijit C., Vimolnoch M., Suriyapee S., Saksornchai K., Estimated radiation doses to ovarian and uterine organs in breast cancer irradiation using radio-photoluminescent glass dosimeters (RPLDs), J Med Radiat Sci. 68(2021) 167– 174

4. Oonsiri P, Nantavithya C, Lertbutsayanukul C, Sarsitthithum T,

Vimolnoch M, Tawonwong T, Saksornchai K. Dosimetric evaluation of photons versus protons in postmastectomy planning for ultrahypofractionated breast radiotherapy. Radiat Oncol. 2022 Jan 29;17(1):20. doi: 10.1186/s13014-022-01992-w. PMID: 35093111; PMCID: PMC8799967.

5. Intarak S, Chongpison Y, Vimolnoch M, Oonsiri S, Kitpanit S, Prayongrat A, Kannarunimit D, Chakkabat C, Sriswasdi S, Lertbutsayanukul C, Rakvongthai Y. Tumor Prognostic Prediction of Nasopharyngeal Carcinoma Using CT-Based Radiomics in Non-Chinese Patients. Front Oncol. 2022 Jan 28;12:775248. doi: 10.3389/fonc.2022.775248. PMID: 35155228; PMCID: PMC8831248.

6. Vimolnoch, M., Israngkul Na Ayuthaya , I. ., Kingkaew, S. ., & Oonsiri, S. (2022). Evaluation of the Varian TrueBeam™ 6 MV phase-space files for the Monte Carlo simulation in small field dosimetry. Journal of Associated Medical Sciences, 55(3), 26–35.